Journal Pre-proof

A two-dimensional double layer-averaged model of hyperconcentrated turbidity currents with non-Newtonian rheology

Yining Sun, Ji Li, Zhixian Cao, Alistair G.L. Borthwick

PII: S1001-6279(23)00050-1

DOI: https://doi.org/10.1016/j.ijsrc.2023.08.002

Reference: IJSRC 506

To appear in: *International Journal of Sediment Research*

Received Date: 11 January 2023

Revised Date: 8 August 2023

Accepted Date: 16 August 2023

A two-dimensional double layer-averaged model of hyperconcentrated turbidity currents with non-Newtonian rheology

Yining Sun[a], Ji Li[b], Zhixian Cao[a,*], Alistair G. L. Borthwick[c,d]

[a] State Key Laboratory of Water Resources Engineering and Management, Wuhan University, Wuhan 430072, China

[b] Zienkiewicz Centre for Computational Engineering, Faculty of Science and Engineering, Swansea University, Swansea SA1 8EN, UK

[c] Institute for Infrastructure and Environment, University of Edinburgh, Edinburgh EH9 3JL, UK

[d] School of Engineering, Computing and Mathematics, University of Plymouth, Plymouth PL4 8AA, UK

* Corresponding author

E-mail: zxcao@whu.edu.cn (Z. Cao)

A two-dimensional double layer-averaged model of hyperconcentrated turbidity currents with non-Newtonian rheology

ABSTRACT

Hyperconcentrated turbidity currents typically display non-Newtonian characteristics that influence sediment transport and morphological evolution in alluvial rivers. However, hydro-sediment-morphological processes involving hyperconcentrated turbidity currents are poorly understood, with little known about the effect of the non-Newtonian rheology. The current paper extends a recent two-dimensional double layer-averaged model to incorporate non-Newtonian constitutive relations. The extended model is benchmarked against experimental and numerical data for cases including subaerial mud flow, subaqueous debris flow, and reservoir turbidity currents. The computational results agree well with observations for the subaerial mud flow and independent numerical simulations of subaqueous debris flow. Differences between the non-Newtonian and Newtonian model results become more pronounced in terms of propagation distance and sediment transport rate as sediment concentration increases. The model is then applied to turbidity currents in the Guxian Reservoir planned for middle Yellow River, China, which connects to a tributary featuring hyperconcentrated sediment-laden flow. The non-Newtonian model predicts slower propagation of turbidity currents and more significant bed aggradation at the confluence between the tributary Wuding River and the Yellow River in the reservoir

than its Newtonian counterpart. This difference in model performance could be of considerable importance when optimizing reservoir operation schemes.

KEYWORDS

Double layer-averaged model; Non-Newtonian rheology; Mud flow; Reservoir turbidity current; Yellow River

1. Introduction

Turbidity currents are subaqueous sediment-laden flows driven by the difference in density between the current and the overlying ambient fluid. Hyperconcentrated turbidity currents carrying fine sediment at concentrations exceeding 200–300 $\mathrm{kg/m^3}$ typically demonstrate non-Newtonian behavior, especially in the ocean and sandy rivers (Cao et al., 2006; Wang et al., 2009). Examples include submarine sediment slumping on continental slopes and subaerial sediment-laden flows plunging into reservoirs. Submarine mud flows with massive momentum may cause severe damage to offshore structures, subsea pipelines, and communication cables, and even trigger tsunamis (Qian et al., 2020). Reservoir turbidity currents in alluvial rivers may lead to abnormal hydro-sediment-morphological characteristics in reservoirs, such as enhanced sedimentation and, consequently, high flood levels (Wang et al., 2007). In such cases, a mathematical model capable of simulating hyperconcentrated turbidity currents is essential for river management. Prime examples are found in the Yellow River and its tributaries in China, where volumetric sediment concentration can reach 0.3 or higher during a flood event (Zhang & Xie, 1993).

In practice, it is difficult to measure the hydro-sediment-morphological processes of turbidity currents with high sediment concentrations in the field (Wright et al., 1988). Unlike the numerous laboratory experiments concerning dilute turbidity currents that exhibit Newtonian behavior (Fedele & García, 2009; Lee & Yu, 1997), only a few attempts have been made to study turbidity currents or mud flows with high sediment concentrations exhibiting non-Newtonian behavior (Hallworth & Huppert, 1998; Jacobson & Testik, 2013). Numerical modelling, therefore, provides a very useful means of studying non-Newtonian, hyperconcentrated turbidity currents.

At present, full three-dimensional models incur excessive computational costs and are not feasible for large-scale, long-duration simulations (Denlinger & Iverson, 2001; Georgoulas et al., 2010; Wang et al., 2016). Many one-dimensional models have been proposed to investigate hyperconcentrated sediment-laden flows (Brufau et al., 2000; Guo et al., 2008; Imran et al., 2001; Xia & Tian, 2022). Such models neglect interactions between subaqueous flows and the ambient fluid, and are inherently unable to simulate lateral spreading. For example, Imran et al. (2001) numerically solved the continuity and momentum equations for a mud flow incorporating either Herschel–Bulkley or bilinear rheology, while neglecting the spatiotemporal variation in sediment concentration and the feedback effect from morphological evolution. Two-dimensional (2D) layer-averaged models offer a compromise between computational expense and theoretical accuracy, and thus, are more suitable for the simulation of hyperconcentrated turbidity currents. Even so, the majority of such models are limited to a single layer or based on an empirical plunge criterion, whereby only the subaqueous sediment-laden flow layer is modeled, and movement of the upper ambient fluid is neglected (Adebiyi & Hu, 2021; Hu et al., 2012; Hu & Li, 2020; Lai et al., 2015), or differences between incipient and stable plunge criteria are ignored (Wang et al., 2016, 2018). Those models are restricted to modeling the propagation of reservoir turbidity currents after their formation, as the upper clear-water flow is ignored and not modeled at all.

Physically, the vertically sharply stratified flow structure, comprising an upper clear-water flow layer and a lower sediment-laden flow layer (turbidity currents) explicitly necessitates a double layer-averaged modeling framework. To the authors' knowledge, the coupled 2D double layer-averaged model proposed by Cao et al. (2015) is uniquely capable of resolving the whole processes of dilute reservoir turbidity currents from formation and propagation to recession, as well as bed evolution. This model, along with its original and recent extended versions, has been applied to resolve dam-break floods over erodible beds, landslide-generated waves, and barrier lake formation and breach processes (Li et al., 2013, 2019, 2020, 2021). However, the model neglects non-Newtonian characteristics of turbidity currents with high sediment concentrations.

In practice, the viscosity of a hyperconcentrated turbidity current alters according to the material strain rate, and so its rheology obeys a non-Newtonian constitutive law, which is quite distinct from that of a dilute flow. Experimental studies have revealed that the rheology of non-Newtonian flows can be approximately expressed using linear (e.g., Bingham), non-linear (Balmforth & Provenzale, 2010; Huang & Garcia, 1997; Imran et al., 2001; O'Brien & Julien, 1988), or bilinear constitutive (Locat, 1997) laws. Among these viscoplastic models, the Herschel–Bulkley model, which incorporates the effects of both shear thinning and yield stress, is most generally suitable for expressing the non-linear characteristics of non-Newtonian flows. Physically, shear thinning and yield stress effects are fundamentally responsible for the rheological differences between Newtonian and non-Newtonian flows. The rheological properties of hyperconcentrated turbidity currents also significantly influence the suspension state of sediment particles, sediment exchange between the flow and the mobile bed, and sediment transport.

Although numerous studies on turbidity currents have examined dilute mixtures exhibiting Newtonian behavior (Cao et al., 2015; Fedele & García, 2009; Hu & Li, 2020; Lee & Yu, 1997), previous layer-averaged models incorporating non-Newtonian rheology have been confined to a single layer (Hu & Li, 2020; Lai et al., 2015) neglecting the movement of upper layer. In actuality, both non-Newtonian rheology and inter-layer interactions are crucial to the evolution of a hyperconcentrated turbidity current. Therefore, we extend the double layer-averaged model proposed by Cao et al. (2015) from dilute to hyperconcentrated currents by incorporating two essential non-Newtonian properties.

Herein, the extended model is benchmarked against a portfolio of experimental and numerical cases, including subaerial mud flow (Wright, 1987), subaqueous debris flow (Imran et al., 2001), and reservoir turbidity currents (Wang et al., 2020). A field-scale numerical study also is done for a large-scale, long-duration turbidity current in the Guxian

Reservoir planned for the Yellow River, to demonstrate the capability of the proposed extended model. The overall aim of the extended model is to provide insight into the underlying effects of rheology on hydro-sediment-morphological processes related to hyperconcentrated turbidity currents in sediment-laden rivers. Such insight is essential for the optimization of reservoir operation schemes where hyperconcentrated turbidity currents may occur.

2. Mathematical model

2.1. Governing equations

In this section, an extended double layer-averaged (EDL) model is developed by modifying the original double layer-averaged (ODL) model proposed by Cao et al. (2015) to include the rheological effect of a non-Newtonian fluid. Among the many formulations proposed for non-Newtonian rheology, the most common approximations for the non-Newtonian shear stress τ_{B} are given by the Bingham, Herschel–Bulkley, and bilinear constitutive models (Locat, 1997). Herein, the Herschel–Bulkley model, which explicitly incorporates primary non-Newtonian effects, i.e., shear-thinning and yield-stress, is selected:

$$\begin{cases} \tau_{\mathrm{B}} = \left(\tau_{\mathrm{Y}} + \mu_{\mathrm{Y}} |\gamma|^{n}\right) \mathrm{sgn}(\gamma), & |\tau_{\mathrm{B}}| > \tau_{\mathrm{Y}} \\ \gamma = 0, & |\tau_{\mathrm{B}}| \le \tau_{\mathrm{Y}} \end{cases} \tag{1}$$

where τ_{Y} is the yield stress; $\gamma = \dfrac{\partial u}{\partial z}$ is the shear rate; μ_{Y} is the fluid consistency; and the power index $n = 1$ denotes a linear Bingham model, $n < 1$ denotes a shear-thinning model, and $n > 1$ denotes a shear-thickening model.

The EDL model comprises: (i) an upper clear-water flow layer; (ii) a lower sediment-laden flow layer (i.e., turbidity current); and (iii) an erodible bed with vanishing velocity (see Fig. S1 in the Supporting Materials). In the derivation of governing equations of the proposed model, a mild slope assumption and shallow water approximations are utilized, while the diffusion effects are tentatively neglected (Wu, 2007) (see Supporting Materials for the detailed derivation). The governing equations of the EDL model are the 2D shallow water equations comprising the mass and momentum conservation equations for the upper clear-water flow layer, respectively, and the mass and momentum conservation equations incorporating the Herschel–Bulkley model for the lower sediment-laden flow layer, and also the mass conservation equations for sediment in the sediment-laden flow layer and bed sediment, respectively. These equations are as follows.

For the upper clear-water flow layer:

$$\frac{\partial \eta}{\partial t}+\frac{\partial h_{\mathrm{w}} U_{\mathrm{w}}}{\partial x}+\frac{\partial h_{\mathrm{w}} V_{\mathrm{w}}}{\partial y}=-E_{\mathrm{w}}+\frac{\partial \eta_{\mathrm{s}}}{\partial t} \tag{2}$$

$$\frac{\partial h_{\mathrm{w}} U_{\mathrm{w}}}{\partial t}+\frac{\partial}{\partial x}\left[h_{\mathrm{w}} U_{\mathrm{w}}^{2}+0.5 g\left(\eta^{2}-2 \eta \eta_{\mathrm{s}}\right)\right]+\frac{\partial}{\partial y}\left(h_{\mathrm{w}} U_{\mathrm{w}} V_{\mathrm{w}}\right)=-\frac{\tau_{\mathrm{wx}}}{\rho_{\mathrm{w}}}-g \eta \frac{\partial \eta_{\mathrm{s}}}{\partial x}-E_{\mathrm{w}} U_{\mathrm{w}} \tag{3}$$

$$\frac{\partial h_{\mathrm{w}} V_{\mathrm{w}}}{\partial t}+\frac{\partial}{\partial x}\left(h_{\mathrm{w}} U_{\mathrm{w}} V_{\mathrm{w}}\right)+\frac{\partial}{\partial y}\left[h_{\mathrm{w}} V_{\mathrm{w}}^{2}+0.5 g\left(\eta^{2}-2 \eta \eta_{\mathrm{s}}\right)\right]=-\frac{\tau_{\mathrm{wy}}}{\rho_{\mathrm{w}}}-g \eta \frac{\partial \eta_{\mathrm{s}}}{\partial y}-E_{\mathrm{w}} V_{\mathrm{w}} \tag{4}$$

For the lower sediment-laden flow layer-turbidity currents:

$$\frac{\partial \eta_{\mathrm{s}}}{\partial t}+\frac{\partial h_{\mathrm{s}} U_{\mathrm{s}}}{\partial x}+\frac{\partial h_{\mathrm{s}} V_{\mathrm{s}}}{\partial y}=E_{\mathrm{w}} \tag{5}$$

$$\begin{aligned}
&\frac{\partial h_{\mathrm{s}} U_{\mathrm{s}}}{\partial t}+\frac{\partial}{\partial x}\left[h_{\mathrm{s}} U_{\mathrm{s}}^{2}+0.5 g\left(\eta_{\mathrm{s}}^{2}-2 \eta_{\mathrm{s}} z_{\mathrm{b}}\right)\right]+\frac{\partial}{\partial y}\left(h_{\mathrm{s}} U_{\mathrm{s}} V_{\mathrm{s}}\right)=-g \eta_{\mathrm{s}} \frac{\partial z_{\mathrm{b}}}{\partial x}-\frac{\rho_{\mathrm{w}} g}{\rho_{\mathrm{c}}} h_{\mathrm{s}} \frac{\partial h_{\mathrm{w}}}{\partial x} \\
&-\frac{\left(\rho_{0}-\rho_{\mathrm{c}}\right)(E-D) U_{\mathrm{s}}}{(1-p) \rho_{\mathrm{c}}}+\frac{\left(\rho_{\mathrm{s}}-\rho_{\mathrm{w}}\right) c_{\mathrm{s}} U_{\mathrm{s}} E_{\mathrm{w}}}{\rho_{\mathrm{c}}}+\frac{\rho_{\mathrm{w}} E_{\mathrm{w}} U_{\mathrm{w}}}{\rho_{\mathrm{c}}}-\frac{\left(\rho_{\mathrm{s}}-\rho_{\mathrm{w}}\right) g h_{\mathrm{s}}^{2}}{2 \rho_{\mathrm{c}}} \frac{\partial c_{\mathrm{s}}}{\partial x} \\
&+\frac{\tau_{\mathrm{wx}}}{\rho_{\mathrm{c}}}-\beta_{\mathrm{N}} \frac{\tau_{\mathrm{N}x}}{\rho_{\mathrm{c}}}-\frac{\beta_{\mathrm{B}}}{\rho_{\mathrm{c}}}\left[\left(\frac{\tau_{\mathrm{Y}}}{\left|\gamma_{x}\right|}+\mu_{\mathrm{Y}}\left|\gamma_{x}\right|^{n-1}\right) \gamma_{x}\right]\bigg|_{z=z_{\mathrm{b}}}
\end{aligned} \tag{6}$$

$$\frac{\partial h_s V_s}{\partial t} + \frac{\partial}{\partial x}\left(h_s U_s V_s\right) + \frac{\partial}{\partial y}\left[h_s V_s^2 + 0.5g\left(\eta_s^2 - 2\eta_s z_b\right)\right] = -g\eta_s \frac{\partial z_b}{\partial y} - \frac{\rho_w g}{\rho_c} h_s \frac{\partial h_w}{\partial y}$$
$$-\frac{\left(\rho_0 - \rho_c\right)\left(E - D\right)V_s}{\left(1-p\right)\rho_c} + \frac{\left(\rho_s - \rho_w\right)c_s V_s E_w}{\rho_c} + \frac{\rho_w E_w V_w}{\rho_c} - \frac{\left(\rho_s - \rho_w\right) g h_s^2}{2\rho_c}\frac{\partial c_s}{\partial y} \quad (7)$$
$$+\frac{\tau_{wy}}{\rho_c} - \beta_N \frac{\tau_{Ny}}{\rho_c} - \frac{\beta_B}{\rho_c}\left[\left(\frac{\tau_Y}{\left|\gamma_y\right|} + \mu_Y \left|\gamma_y\right|^{n-1}\right)\gamma_y\right]\Bigg|_{z=z_b}$$

$$\frac{\partial h_s c_s}{\partial t} + \frac{\partial h_s U_s c_s}{\partial x} + \frac{\partial h_s V_s c_s}{\partial y} = E - D \quad (8)$$

For bed sediment:

$$\frac{\partial z_b}{\partial t} = -\frac{E-D}{1-p} \quad (9)$$

where t is time; g is the acceleration due to gravity; x and y are the horizontal coordinates; h_w is the thickness of the upper clear-water flow layer; h_s is the thickness of the lower sediment-laden flow layer; c_s is the volumetric sediment concentration; U_w and V_w are clear-water flow layer-averaged velocity components in the *x*- and *y*-directions, respectively; U_s and V_s are the sediment-laden flow layer-averaged velocity components in the *x*- and *y*-directions, respectively; z_b is the bed elevation; η is the elevation of the water surface above a fixed horizontal datum; η_s is the elevation of the interface between the clear-water and sediment-laden flow layers above the same datum; ρ_w is the density of water; ρ_s is sediment density; $\rho_c = \rho_w(1-c_s) + \rho_s c_s$ is the density of the water–sediment mixture in the turbidity current layer; p is the bed sediment porosity; $\rho_0 = \rho_w p + \rho_s(1-p)$ is the density of the saturated bed; τ_{wx} and τ_{wy} are the shear stresses at the interface between the clear-water and sediment-laden flow layers in the *x*- and *y*-directions, respectively; E_w is water entrainment flux across the interface between the two layers; β_B and β_N are the coefficients introduced to control the

Newtonian or non-Newtonian behavior according to sediment concentration; τ_{Nx} and τ_{Ny} are the shear stresses due to Newtonian rheology in the *x*- and *y*-directions, respectively; γ_x and γ_y are the near-bed shear rates in the *x*- and *y*-directions, respectively; E and D are the sediment entrainment flux and sediment deposition flux, respectively.

The effective shear stress is defined as $\tau_{\text{eff}} = -\left(\beta_B \tau_B + \beta_N \tau_N\right)$. In practice, hyperconcentrated flows with non-Newtonian rheology may eventually transform into Newtonian fluids in cases where the current is sufficiently dilute (Pierson & Scott, 1985). Experimental studies have collectively shown that $\beta_B = 0$ and $\beta_N = 1$ for a "Newtonian" water–sediment mixture with low sediment concentration (less than the threshold concentration transformed from the Newtonian fluid to non-Newtonian fluid, which is defined in Section 2.2). When the sediment concentration is higher than the threshold concentration, the lower sediment-laden flow layer acts as a non-Newtonian fluid, such that $\beta_B = 1$ and $\beta_N = 0$.

2.2. Model closure

To close the governing equations, a set of relations is introduced to determine the water entrainment, E_w, sediment exchange fluxes (i.e., entrainment flux E, minus deposition flux D), interface shear stress, and bed boundary resistance, as per Cao et al. (2015). Following Parker et al. (1986), the water entrainment mass flux, E_w, is calculated from

$$E_w = e_w \overline{U}_{ws} \tag{10}$$

where $\overline{U}_{ws} = \sqrt{(U_w - U_s)^2 + (V_w - V_s)^2}$ is the magnitude of the resultant velocity difference between the two layers; and the water entrainment coefficient e_w is estimated from

$$e_{\mathrm{w}} = \frac{0.00153}{0.0204 + Ri} \tag{11}$$

in which the Richardson number $Ri = sgc_{\mathrm{s}}h_{\mathrm{s}} / \overline{U}_{\mathrm{ws}}^2$ and the specific gravity of sediment $s = \rho_{\mathrm{s}} / \rho_{\mathrm{w}} - 1$. Eqs. (12) and (13) are used to calculate the sediment entrainment and deposition fluxes:

$$D = \omega c_{\mathrm{s}} \left(1 - c_{\mathrm{s}}\right)^m \tag{12}$$

$$E = \omega E_{\mathrm{s}} \tag{13}$$

where $\omega(1 - c_{\mathrm{s}})^m$ is the hindered sediment settling velocity in Eq. (12), using the relation determined by Richardson and Zaki (1997). The power *m* is estimated from $m = 4.45R_{\mathrm{p}}^{-0.1}$, in which $R_{\mathrm{p}} = \omega d / \nu$ is the particle Reynolds number, where ω is the settling velocity of a single sediment particle in tranquil clear water, calculated using the formula of Zhang and Xie (1993) as

$$\omega = \sqrt{\left(13.95\frac{\nu}{d}\right)^2 + 1.09sgd} - 13.95\frac{\nu}{d} \tag{14}$$

where *d* is the sediment particle diameter and ν is the kinematic viscosity of water.

It is noted that, an appropriate formula for the sediment entrainment flux for cohesive sediment has, to date, remained missing in line with non-Newtonian rheology. In evaluating Eq. (13), the empirical formula in Eq. (15) proposed by Zhang and Xie (1993), which is well-tested and widely used for suspended sediment transport, including for the Yellow River, China, is tentatively applied:

$$E_{\mathrm{s}} = \frac{1}{20\rho_{\mathrm{s}}} \frac{(\overline{U}_{\mathrm{s}}^3 / gh_{\mathrm{s}}\omega)^{1.5}}{1 + (\overline{U}_{\mathrm{s}}^3 / 45gh_{\mathrm{s}}\omega)^{1.15}} \tag{15}$$

Manning's formula is used to calculate resistance relations between the upper layer clear water flow, the lower layer sediment-laden flow, and the erodible bed as Eqs. (16)–(20) (Cao et al., 2015):

$$\tau_{wx} = \rho_w g n_i^2 (U_w - U_s)\overline{U}_{ws} / h_w^{1/3} \tag{16}$$

$$\tau_{wy} = \rho_w g n_i^2 (V_w - V_s)\overline{U}_{ws} / h_w^{1/3} \tag{17}$$

$$\tau_{Nx} = \rho_c g n_b^2 U_s \overline{U}_s / h_s^{1/3} \tag{18}$$

$$\tau_{Ny} = \rho_c g n_b^2 V_s \overline{U}_s / h_s^{1/3} \tag{19}$$

where n_i is Manning's coefficient representing friction at the interface between the sediment-laden flow layer and clear-water flow layer; n_b is Manning's coefficient representing bed roughness; and $\overline{U}_s = \sqrt{U_s^2 + V_s^2}$ is the resultant velocity of the sediment-laden flow layer.

The equation derivations involve a rheological model that represents non-Newtonian fluid characteristics through the effective bed shear stress τ_{eff}. One of the pivotal issues in non-Newtonian fluid simulation is the estimation of the yield stress τ_{Y}, and viscous stress $\tau_{\text{V}}\left(= \mu_{\text{Y}}\gamma^n\right)$, which are determined either by calibration against measured data or by using empirical relations, such as the formulae proposed by Fei et al. (1991):

$$\tau_{\text{Y}} = 0.098\exp\left(8.45\frac{c_{\text{s}} - c_{\text{v0}}}{c_{\text{vm}}} + 1.5\right) \tag{20}$$

$$\mu_{\text{Y}} = \mu_0\left(1 - k\, c_{\text{s}}/c_{\text{vm}}\right)^{-2.5} \tag{21}$$

where the sediment limiting concentration $c_{\text{vm}} = \phi\left(0.92 + 0.02\log\left(1/d\right)\right)$, with a correction coefficient ϕ to account for the limited number of sediment samples used in devising the original relation; the threshold concentration from the Newtonian fluid to non-Newtonian fluid, $c_{\text{vo}} = 1.26 c_{\text{vm}}^{3.2}$; the coefficient $k = 1 + 2.0\left(c_{\text{s}}/c_{\text{vm}}\right)^{0.3}\left(1 - c_{\text{s}}/c_{\text{vm}}\right)^4$; and μ_0 is the dynamic viscosity of water.

Based on an assumption of a non-linear velocity distribution over the depth (Johnson et al., 2012),

$$u_{si}(z) = (2-\alpha_n)\left[1-\left(1-\frac{z-z_b}{h_s}\right)^{\frac{1}{1-\alpha_n}}\right]U_{si}, \quad i = x,\ y \tag{22}$$

where $u_{si}(z)$ is the vertical velocity distribution; z is the vertical coordinate; α_n is the profile shape parameter; U_{si} is the depth-integrated velocity. Thus, the velocity gradient components of sediment-laden flow at the basal surface (i.e., near-bed shear rates) are approximated by

$$\gamma_x = \left.\frac{\partial u_s}{\partial z}\right|_{z=z_b} = \frac{2-\alpha_n}{1-\alpha_n}\frac{U_s}{h_s}, \quad \alpha_n = [0,\ 1) \tag{23}$$

$$\gamma_y = \left.\frac{\partial v_s}{\partial z}\right|_{z=z_b} = \frac{2-\alpha_n}{1-\alpha_n}\frac{V_s}{h_s}, \quad \alpha_n = [0,\ 1) \tag{24}$$

2.3. Numerical algorithm

The governing equations for the lower sediment-laden flow layer are taken as a nonhomogeneous hyperbolic system, with bed shear stress for non-Newtonian rheology expressed as a source term, thus, preserving hyperbolicity (Li et al., 2015). The two hyperbolic systems of governing equations for the two layers are solved separately and synchronously. Each hyperbolic system is solved by a quasi-well balanced numerical algorithm involving drying and wetting, using a second-order accurate, finite volume Godunov-type approach in conjunction with the Harten–Lax–van Leer contact wave (HLLC) approximate Riemann solver (Toro, 2001) on a fixed rectangular mesh. Assuming that bed deformation is entirely determined by local entrainment and deposition fluxes in accordance with the non-capacity model of sediment transport, Eq. (9) is solved separately from the remaining equations. A detailed description of the numerical algorithm is given by Cao et al. (2015).

3. Benchmark tests

A series of experimental and numerical benchmark tests is used to validate the proposed EDL model for subaerial mud flow (Wright, 1987) (see Section S2 in the Supporting Materials), subaqueous debris flow, and reservoir turbidity current. In all cases, fixed uniform meshes are applied, and refined to ensure mesh independence. The Courant number is set to 0.4, bed porosity $p = 0.4$, and the profile shape parameter $\alpha_n = 0$. To quantify discrepancies between computational results and experimental data, the coefficient of determination (R^2) is calculated as Eq. (25):

$$R^2 = \frac{\left[\sum_{i=1}^{n}\left(E_i^{\text{obs}} - \bar{E}^{\text{obs}}\right)\left(E_i^{\text{com}} - \bar{E}^{\text{com}}\right)\right]^2}{\sum_{i=1}^{n}\left(E_i^{\text{obs}} - \bar{E}^{\text{obs}}\right)^2 \sum_{i=1}^{n}\left(E_i^{\text{com}} - \bar{E}^{\text{com}}\right)^2} \tag{25}$$

where E_i^{obs} represents observed data i, and $\bar{E}^{\text{obs}}$ is the mean value of the observed values; E_i^{com} represents computed data i, and $\bar{E}^{\text{com}}$ is the mean value of the computed values. The closer R^2 is to 1, the smaller the discrepancy.

3.1. Subaqueous debris flow

A numerical case originally examined by Imran et al. (2001) is first used to probe into the choice of the rheological model on the evolution of subaqueous debris flow. The flow domain comprises a 7,200 m long rectangular flume, whose bottom slope is 0.05. The following parameters are specified according to Run AQ of Imran et al. (2001): initial profile of slurry thickness is parabolic of length $L = 600\,\mathrm{m}$ and maximum thickness $h_{s0} = 24\,\mathrm{m}$ at the centre, corresponding to Fig. S4 in the Supporting Materials; the initial density of the debris flow is $\rho_{c0} = 1{,}500\,\mathrm{kg/m^3}$; and the debris flow has Bingham rheology (i.e., $n = 1$ in the Herschel–Bulkley model), with yield stress $\tau_Y = 1{,}000\,\mathrm{N/m^2}$ and a dynamic viscosity $\mu_Y = 400\,\mathrm{N \cdot s/m^2}$. Grid spacing is 2 m in both longitudinal and lateral directions. Solid boundary conditions for the upper clear-water flow layer and the lower sediment-laden flow layer are implemented through the flux computation approach suggested by Hou et al. (2013).

3.1.1. Model Comparison

Simulations are done using the proposed EDL model for the same failure volume, yield stress, and dynamic viscosity as Imran et al.'s (2001) model. It should be noted that Imran et al.'s model is applicable only to subaqueous debris flows over a fixed bed and does not account for inter-layer interactions and bed deformation. Hence, water entrainment E_w, interface friction resistance τ_w, and sediment entrainment and deposition fluxes of the proposed EDL model are all set to zero for the validation test.

Fig. 1 shows the comparison of the computed thickness of the debris flows obtained with the proposed EDL model (with a Bingham rheological relation) with the numerical predictions of Imran et al. (2001). The results are presented in non-dimensional form, based on the following horizontal and vertical scales, $L = 600\,\mathrm{m}$ and $h_{s0} = 24\,\mathrm{m}$. In the original numerical case, the initial ambient water depth is difficult to discern, and its effect on the debris flow is negligible (see Fig. S5 in the Supporting Materials); herein, the initial ambient water depth is set to $50\,h_{s0}$. Fig. 1 shows that the subaqueous debris flows computed using Imran et al.'s (2001) model and the proposed EDL model yield almost identical profiles. At $t = 2\,\text{min}$, the thickness of debris flow computed using the proposed EDL model is larger in the front and smaller in the tail than that calculated with Imran et al.'s (2001) model, whereas the runout distances are nearly identical (Fig. 1(a)). At $t = 22\,\text{min}$, the final runout distance computed using the proposed EDL model is marginally longer than that determined by Imran et al.'s (2001) model (Fig. 1(b)). From Fig. 1, the computed evolution of the debris flow obtained from both models shows reasonable agreement. Slight differences between the computed profiles mainly arise from the distinct physical mechanisms on which the two models are based. In Imran et al.'s (2001) model, the debris flow is vertically separated into two zones (i.e., plug layer and shear layer), which requires a series of tuning parameters to have to be implemented, whereas such treatment is not necessary for the proposed EDL model.

Fig. 1. Dimensionless thickness of a debris flow computed using Imran et al.'s (2001) model and the proposed EDL model. Water entrainment E_w, interface friction resistance τ_w, and sediment exchange fluxes are set to zero in the proposed EDL model.

3.1.2. Sensitivity analysis

The sensitivity of the computational predictions made using the proposed EDL model to the choice of yield stress τ_Y and power index n is investigated. Firstly, n is set to 1 as in the original numerical case, and spatiotemporal variation of the debris flow is computed for τ_Y = 0, 500, and $1{,}000\ \mathrm{N/m^2}$. Then, the yield stress τ_Y is set to $1{,}000\ \mathrm{N/m^2}$, the same as in the original numerical case, and n is altered by ±0.5.

As the yield stress τ_Y decreases from $1{,}000\ \mathrm{N/m^2}$ to zero, the debris flow progressively acts as a Newtonian flow. Fig. 2 shows the Bingham flow and Newtonian flow profiles at time t = 2 and 22 min. The following differences between the two flow profiles may be discerned. First, the Bingham flow propagates more slowly than the Newtonian flow. Second, the thickness of the Newtonian flow decreases more rapidly with time than that of the Bingham flow, and its surface has a maximum thickness at the front and zero thickness at the tail. Third, the Bingham flow only propagates a finite distance downstream with its front velocity asymptotically falling to zero, whereas the Newtonian flow propagates further downstream. This is primarily because the yield stress of the Bingham flow causes its velocity to decay more rapidly with time than the corresponding Newtonian flow.

The power index n reflects the shear-thinning ($n<1$) or shear-thickening ($n>1$) behavior of a non-Newtonian fluid. Initially, the flow passes through a high shearing rate range, with the power index n representing the extent to which the behavior is non-linear. Here, the viscous stress is higher for larger n, leading to increased thickness and slower propagation of debris flow (Fig. 2(a)). The fluid experiences a low shear rate range during the final period, when the runout distance of the debris flows varies slightly with n, indicating that the evolution of a debris flow due to a low shear rate is almost insensitive to the choice of *n*. The debris flow simulated with $n = 0.5$ propagates furthest downstream (Fig. 2(b)).

Briefly, the dimensionless flow thickness is more sensitive to the yield stress τ_Y. With increased τ_Y, the propagation of the debris flow slows down and the dimensionless flow thickness increases. Moreover, the computed results demonstrate that the empirical parameters involved in the proposed model only affect the computed results to a reasonable extent rather than fundamentally alter the results. Therefore, the choice of the parameters does not affect the current findings.

Fig. 2. Sensitivity of computed dimensionless thickness of debris flow to choice of yield stress τ_Y, and power index n, at time: (a) $t = 2\ \text{min}$ and (b) $t = 22\ \text{min}$. Note that $n = 1$ denotes a linear Bingham model, $n < 1$ represents shear-thinning behavior, and $n > 1$ denotes shear-thickening behavior.

3.1.3. Effect of interaction between two layers on debris flow evolution

The subaqueous debris flow is vertically stratified, characterized by a double-layer flow structure composed of a subaqueous sediment-laden flow layer immediately above the bed and an upper clear-water flow layer. However, Imran et al.'s (2001) model neglected the effect of inter-layer interactions between the two layers, including water exchange E_w, from the upper layer to the lower layer, and interfacial resistance τ_w, both of which are critical for the evolution of a subaqueous debris flow. Fig. 3 shows the effect of interactions between two layers on the evolution of a debris flow. It can be seen that the thickness of the debris flow decreases as it propagates downstream, owing to current spreading and water entrainment. Initially, the debris flow spreads rapidly, and its thickness decreases with distance. When the effect of water entrainment is included, the interface area between the debris flow and the ambient water increases with time, and so the total amount of water entrained increases. Hence, cases accounting for water entrainment exhibit a larger thickness of debris flow at the front and a longer final runout distance than those without. As Manning's roughness coefficient is altered, the debris flow experiences marginally different evolution, indicating that the interfacial resistance τ_w, plays a secondary role (Fig. 3).

Fig. 3. Debris flow profiles predicted using the proposed EDL model for different interface Manning's roughness coefficient values n_i = 0, 0.003, and 0.006 $m^{-1/3} \cdot s$ at time: (a) $t = 2\ \text{min}$ and (b) $t = 22\ \text{min}$.

3.1.4. Effect of particle sedimentation on debris flow evolution

Debris flows with high sediment concentration may drive active morphological evolution featuring intensive, complex interactions between the flow and the bed, which are in turn significant for debris flow evolution. On the one hand, flow stream characteristics, such as density, velocity, and depth, are directly altered by sediment deposition and entrainment. On the other hand, the deformed bed provides morphological feedback to the evolution of the debris flow. However, in Imran et al.'s (2001) model bed deformation caused by sediment deposition or entrainment is ignored; this omission warrants further discussion.

Figs. 4 and 5 show the evolution of the debris flow, bed deformation, and volumetric sediment concentration c_{s}, profiles along the channel at two instants, computed for sediment particle diameter values of $d = 9\,\mu\mathrm{m}$, $62.5\,\mu\mathrm{m}$, and 2 mm. Fig. 4 shows the dimensionless bed deformation $\hat{z}_{\mathrm{b}} = (z_{\mathrm{b}} - z_0)/h_{\mathrm{s0}}$ and dimensionless interface elevation $\hat{\eta}_{\mathrm{s}} = h_{\mathrm{s}}/h_{\mathrm{s0}} + \hat{z}_{\mathrm{b}}$ (where z_0 denotes initial bed elevation) as functions of distance along the channel. At $t = 22\,\mathrm{min}$ (Fig. 4(a)), much of the sediment settles in the tail of the debris flow obtained for particles of large diameter $d = 2\,\mathrm{mm}$ and the deposition thickness decreases in the direction of the debris flow as it propagates downstream. For finer particles, sedimentation is not apparent. Accordingly, the volumetric sediment concentration of the debris flow decreases progressively as the particle diameter increases (Fig. 5). At t = 50 min, the debris flow for $d = 2\,\mathrm{mm}$ slows down. Its sediment particles are all deposited, corresponding to a state of recession of the debris flow (Fig. 4(b)). This occurs primarily because bed and interface resistances dissipate the kinetic energy of the debris flow, and water entrained from the ambient fluid dilutes the water-sediment mixture, thus, reducing the driving force. By contrast, a debris flow with fine particles produces little sedimentation.

Bed deformation is sensitive to sediment particle diameter, with feedback on the debris flow as it evolves. Specifically, as d increases, the sediment deposition thickness grows, runout distance shortens, and volumetric sediment concentration c_{s} reduces; and so there is a smaller driving force for the debris flow. In short, debris flow with larger d

propagates slower.

Fig. 4. Dimensionless free surface level $\hat{\eta}_\mathrm{s} = h_\mathrm{s}/h_\mathrm{s0} + \hat{z}_\mathrm{b}$ and dimensionless bed deformation $\hat{z}_\mathrm{b} = (z_\mathrm{b} - z_0)/h_\mathrm{s0}$ spatial profiles of debris flow, predicted for three values of sediment particle diameter d at time (a) t = 22 min and (b) t = 50 min.

Fig. 5. Volumetric sediment concentration, c_s, spatial profile of debris flow, for three values of sediment particle diameter d at time t = 22 min and 50 min.

3.2. Laboratory-scale turbidity current

As a subaerial sediment-laden flow enters a reservoir, it may plunge under overlying water to form a subaqueous sediment-laden flow called a turbidity current. In theory, a turbidity current with high sediment concentration may exhibit non-Newtonian behavior, unlike a dilute turbidity current which exhibits almost Newtonian behavior. The second set of validation tests relates to a series of physical experiments on tributary turbidity currents done by Wang et al. (2020) using a glass flume, which contained a main channel (0.45 m wide, 30 m long, bed slope $i_\mathrm{bm} = 0.015$) and a tributary (0.3 m wide, 10 m long, bed slope $i_\mathrm{bt} = 0.005$) joined at 90° to the main channel of a distance of 20 m from the outlet of main channel, as shown in Fig. S6 in the Supporting Materials.

Table 1. Selected cases for reservoir turbidity currents (Series E from Wang et al. (2020),

and series D hypothetical).

Series	Case	Q_t (L/s)	C_t $\left(\mathrm{kg/m^3}\right)$	h_{si} (m)
E	E1	1.98	300	0.17
	E2	4	300	0.21
D	D1	4	600	0.21

Table 1 lists key flow parameters for two experimental cases, E1 and E2 (taken from Wang et al., 2020), and one hypothetical case, D1, the last case corresponding to a relatively highly concentrated sediment-laden tributary inflow. As in the experiments, the numerical flume is initially full of still clear water with the water depth set at 0.45 m at the reservoir-tributary confluence. At the tributary inlet, the prescribed discharge Q_t, thickness h_{si}, and mass sediment concentration C_t (Table 1) of the lower sediment-laden flow layer are kept constant, with no clear-water inflow. At the inlet of the main channel, there is no inflow. At the outlet, a constant free surface level is maintained using a tailgate. At the outlet, a free outflow boundary condition is imposed on the lower sediment-laden flow layer, the thickness of the clear-water flow layer is calculated according to a prescribed free surface level, and the layer-averaged velocity is determined by the method of characteristics. The sediment has properties of suspended material taken from the Yellow River, China, with specific gravity of 2.65 and mean particle diameter of 7 μm. The interface roughness Manning coefficient is set as $n_i = 0.005\,\mathrm{m}^{-1/3}$, following Cao et al. (2015). The grid spacing of Δx and Δy are set to 0.025 m.

3.2.1. Validation for physical experiments

Fig. S7 in the Supporting Materials and Fig. 6 display the measured and computed interface elevation, η_s, profiles along the central axes of the main channel and tributary for cases E1 and E2 with different inflow discharges. The range of the interface elevation, η_s, was recorded at two instants, once when the front of the tributary turbidity current arrived at each cross section and once when it reached a stable state. Because sediment concentrations of tributary inflow in cases E1 and E2 are close to the threshold concentration, c_{vo}, for transformation from a Newtonian fluid to a non-Newtonian fluid, computational results of two models, i.e., the proposed EDL model and ODL model, are compared to measured data. Model calibration is done for the computational results of case E1 (see Fig. S7 in the Supporting Materials), through which Manning's roughness coefficient, $n_b = 0.015\,\mathrm{m}^{-1/3}\cdot\mathrm{s}$, for both the EDL model and ODL model, and the coefficient $\phi = 0.85$ for EDL are utilized. Using the calibrated coefficients, the computational results for Case E2 with a larger discharge Q_t agree well with the measured data for the interface elevation, η_s, as confirmed by the coefficients of determination R^2_{ODL} = 0.982 and R^2_{EDL} = 0.981 (Fig. 6(a)). Comparatively, because the sediment concentration of the tributary inflow in Case E2 is slightly higher than the threshold concentration, c_{vo}, there are marginal differences in interface elevation, η_s, between the ODL model and EDL model results, and the final runout distance in the upstream reach of the main channel (UMC) of the turbidity current predicted by the EDL model is slightly shorter than that predicted by the ODL model (Figs. 6(b) and 6(c)). These results confirm the EDL model is applicable to dilute turbidity currents, which may be assumed to be Newtonian.

Fig. 6. Case E2 with a tributary discharge $Q_{\mathrm{t}} = 4\ \mathrm{L/s}$. (a) Comparison between measured and computed ranges of the interface elevation, η_{s}, at each cross section, (b) ODL model, and (c) EDL model predictions and experimental measurements (Wang et al., 2020) of front elevation and interface elevation profiles along the central axes of the main channel (MC) and tributary (TR) at four times. The UMC and DMC refer to upstream and downstream reaches of the main channel.

3.2.2. Designed cases

Turbidity currents with a high sediment concentration differ substantially from those with dilute sediment concentration. Therefore, unlike experimental cases E1 and E2 involving dilute turbidity currents that are almost Newtonian, the hypothetical case D1 is designed to simulate a turbidity current of relatively high sediment concentration, which exhibits non-Newtonian behavior. This hypothetical case enables basic understanding of hyperconcentrated turbidity currents to be obtained, which should translate to large-scale simulations of hyperconcentrated turbidity currents in natural rivers.

3.2.2.1. Impact of non-Newtonian rheology on turbidity current propagation

Fig. 7 displays the evolution of the interface elevation, η_{s}, in the main channel and tributary for Case D1 computed using the EDL and ODL models. After sustained, sediment-laden inflow from the bottom of the tributary inlet, a turbidity current forms as the turbidity volume slumps into clear water because of the driving force arising from the density difference. Upon the arrival of the turbidity current front at the junction (Figs. 7(a) and 7(b)), the front elevation rises rapidly, and the current propagates simultaneously upstream and downstream along the main channel. The turbidity current front thickness in the downstream reach of the main channel (DMC) increases longitudinally because of water entrainment, while that in the UMC decelerates gradually with time (Fig. 7(c)). By $t = 120\ \mathrm{s}$, the front of the turbidity current in the DMC has been vented through the outlet, whilst the turbidity current front extended in the UMC has stabilized (Fig. 7(d)).

In Fig. 7, pronounced differences are evident in the results produced by the EDL and ODL models. Even though both models utilize the same initial and boundary conditions, the EDL model predicts slower turbidity current propagation in the DMC and smaller final runout distance of the turbidity front in the UMC than the ODL model. This is to be expected because the turbidity current computed using the ODL model is not controlled by yield stress, unlike the EDL model, which facilitates a larger flow velocity and a longer runout distance.

Fig. 7. Distribution of interface elevation, η_s, for Case D1 computed using the ODL and EDL models at time: (a) $t = 20\ \mathrm{s}$, (b) $t = 30\ \mathrm{s}$, (c) $t = 60\ \mathrm{s}$, and (d) $t = 120\ \mathrm{s}$. Abbreviations UMC and DMC refer to upstream and downstream reaches of the main channel, respectively.

3.2.2.2. Impact of non-Newtonian rheology on the velocity field of a turbidity current

The effect of non-Newtonian properties on the magnitude of layer-averaged velocity ($\overline{U_s} = \sqrt{U_s^2 + V_s^2}$) is examined for the sediment-laden flow layer for Case D1 computed using the proposed EDL model and reference (Newtonian) ODL model at time $t = 20, 30, 60$, and 120 s. In both simulations, by t = 30 s, the front of the tributary turbidity current has reached the junction and intrudes into the main channel (propagating upstream and downstream simultaneously). The layer-averaged speed of the turbidity current decreases both as it propagates into the UMC and at the corner of the upstream junction where a small recirculation zone occurs. A second flow separation bubble and a region of maximum flow speed near the middle of the main channel develop immediately downstream of the junction as the turbidity current propagates into the DMC (Figs. 8(a) and 8(b)). The speed of the sediment-laden layer in the UMC is lower than that in the DMC. Arguably, this is because interface shear stresses are larger when the turbidity current from the tributary propagates upstream along the main channel. At $t = 120$ s, the turbidity current speed decreases inside the tributary mouth as the current thickness increases. The turbidity current front extending along the UMC is stable and almost unchanging (Fig. 7), and its speed decreases asymptotically to zero because of energy dissipation. A zone of maximum speed is apparent in the main channel just downstream of the junction.

The EDL and ODL models exhibit similarity in terms of predicted flow structure, even though their estimates of bed shear stress differ. Apparent differences occur in the velocity fields predicted by the EDL and ODL models. The turbidity current predicted by the ODL model has a larger flow speed inside the tributary mouth than that predicted by the EDL model. Moreover, the ODL model results contain a zone of maximum flow speed, which is likely a result of the zero yield stress. Even though the ODL model produces a turbidity current of excessive flow speed that enlarges local friction stresses, it nevertheless confirms the impact of yield stress on the modeling of turbidity currents.

Fig. 8. Velocity fields for turbidity current Case D1 computed using (a, c) the proposed EDL model and (b, d) the ODL model at time $t = 30\ \mathrm{s}$ and $t = 120\ \mathrm{s}$.

3.2.2.3. Impact of non-Newtonian rheology on sediment transport

Figures 9–11 show the effects of non-Newtonian rheology on volumetric sediment concentration, and transverse and longitudinal sediment transport rates per unit channel width for Case D1. As the tributary turbidity current intrudes into the main channel, the volumetric sediment concentration in the main channel decreases longitudinally, and the lowest volumetric sediment concentration occurs at the intrusion front (Fig. 9). The transverse sediment transport rate per unit width $(\mathrm{STR}_y = h_\mathrm{s} c_\mathrm{s} V_\mathrm{s})$ of the turbidity current decreases as it propagates into the main channel (Fig. 10(a)). It exhibits almost no change inside the tributary from 30 to 120 s owing to the imposed steady upstream boundary condition (Figs. 10(b) and 10(c)). The longitudinal sediment transport rate per unit width $(\mathrm{STR}_x = h_\mathrm{s} c_\mathrm{s} U_\mathrm{s})$ of the turbidity current is negative in the UMC and asymptotically approaches zero after it is vented through the outlet, whereas it is positive in the DMC, increasing in the region of maximum velocity but decreasing within the flow separation zone (Fig. 11).

During the first 20 s or so, the turbidity current front with low volumetric sediment concentration reaches the junction and differences between the EDL and ODL model predictions of STR_y and STR_x are small (Figs. 10（a) and 11(a)). However, from 30 to 120 s, even though high volumetric sediment concentration ($c_\mathrm{s} > 0.16$) is more widely distributed in the EDL model than the ODL model predictions, the EDL model estimates of STR_y and STR_x are smaller than that of the ODL model inside the tributary mouth and within the maximum velocity zone. This is primarily because the proposed EDL model rheology facilitates higher bed shear resistance than the ODL model, reducing the flow speed, and, hence, the sediment transport rate.

Fig. 9. Contour plots of volumetric sediment concentration, c_s, for turbidity current Case D1, computed using the ODL and proposed EDL models at time: (a) $t = 20\,\mathrm{s}$, (b) $t = 30\,\mathrm{s}$, (c) $t = 60\,\mathrm{s}$, and (d) $t = 120\,\mathrm{s}$.

Fig. 10. Contour plots of transverse sediment transport rate per unit width, STR_y, near the confluence for Case D1, computed using the proposed EDL and ODL models at time: (a) $t = 20\,\mathrm{s}$, (b) $t = 30\,\mathrm{s}$, (c) $t = 60\,\mathrm{s}$, and (d) $t = 120\,\mathrm{s}$.

Fig. 11. Contour plots of longitudinal sediment transport rate per unit width, STR_x, near

the confluence for Case D1 computed using the proposed EDL and ODL models at time: (a) $t = 20\ \mathrm{s}$, (b) $t = 30\ \mathrm{s}$, (c) $t = 60\ \mathrm{s}$, and (d) $t = 120\ \mathrm{s}$.

3.2.2.4. Impact of non-Newtonian rheology on bed shear stress

It is revealing to investigate differences in bed shear stress computed using the non-Newtonian EDL and Newtonian ODL models. Fig. 12 shows the bed shear stress distribution for Case D1 at time t = 20, 30, 60, and 120 s. By t = 30 s, the tributary turbidity current has reached the junction and intruded into the main channel, and the volumetric sediment concentration near the confluence is approximately equivalent to the threshold concentration c_{vo} (Figs. 9(a) and 9(b)). At the junction, the bed shear stress with non-Newtonian characteristics is similar to that with Newtonian rheology, with the maximum velocity zone experiencing a high level of bed shear stress (Figs. 12(a) and 12(b)). Moreover, the volumetric sediment concentration inside the tributary predicted by the EDL model is higher than that predicted by the ODL model (Fig. 9(b)). Here, the bed shear stress obtained using non-Newtonian rheology is larger than that using Newtonian rheology because of the presence of yield stress (Fig. 12(b)). Later, between t = 60 and 120 s (Figs. 12(c) and 12(d)), the bed shear stress predicted by the ODL model is generally below 1 $\mathrm{N/m^2}$ in the UMC, but reaches about 3.5 $\mathrm{N/m^2}$ in the region of maximum flow speed. The bed shear stress predicted by the EDL model is quite different in that it reaches approximately 2.5 $\mathrm{N/m^2}$ in the UMC, and about 3 $\mathrm{N/m^2}$ in the zone of maximum flow speed. This implies that the bed shear stress magnitude predicted by the proposed EDL model is directly related to the sediment concentration distribution when higher than the threshold concentration, c_{vo}. Conversely, the bed shear stress magnitude predicted by the ODL model is only related to the velocity field of the turbidity current.

Fig. 12. Contours of bed shear stress, τ_{eff}, for Case D1 computed using the proposed EDL and ODL models at time: (a) $t = 20\ \mathrm{s}$, (b) $t = 30\ \mathrm{s}$, (c) $t = 60\ \mathrm{s}$, and (d) $t = 120\ \mathrm{s}$.

4. Model application—Guxian Reservoir, Yellow River

4.1. Study area

The Guxian Reservoir, planned for the middle Yellow River, China, is likely to have tributary sediment inputs that account for more than 40% of the total sediment input (whose volumetric concentration could exceed 0.3) during extreme flood events and behave as a non-Newtonian fluid. The Guxian Reservoir was, therefore, selected for a prototype-scale study. In the proposed computational model, the initial bed topography is estimated from observed data acquired during April 2017. The domain comprises the main channel of the Yellow River from Wubu to the Guxian Dam (approximately 200 km long and 300–1,500 m wide), and a major tributary, the Wuding River, from Baijiachuan to its junction with the main Yellow River. The study reach of the Wuding River is about 17 km long from the junction to Baijiachuan, located about 130 km upstream of the Guxian Dam. Accurate topographic and hydrological data are unavailable for the other tributaries with smaller discharges and lower sediment concentrations, and so these are neglected herein.

4.2. Model setup

Under normal operating conditions, the planned water level in the Guxian Reservoir is 627 m relative to the 1985 National Height Datum, China, corresponding to a total water storage capacity of 12.94×10^9 m^3. A fixed-bed, steady flow simulation first was done for gradually varied, clear-water inflow discharges specified at Wubu and Baijiachuan, and the resulting flow hydrodynamics are taken as the initial condition for the present application of the ODL and EDL models. Table 2 lists the flow discharge and volumetric sediment concentration input values at the two upstream boundary cross sections (i.e., Wubu and Baijiachuan stations, Fig. 13). Noting the availability of observed data for input to the model, the evolution of the turbidity current was simulated for a highly concentrated sediment-laden flood that entered the Guxian Reservoir in July 2017 (Table 2, Wubu, and Fig. 13, Baijiachuan station). At the downstream boundary (Guxian Dam), a boundary condition is not required for the turbidity current before its front arrives. The depth and velocity of the clear-water flow layer are determined by the method of characteristics according to the outflow discharge Q_{out}, which is kept constant at 6,067 m^3/s, the design discharge for Guxian Reservoir.

Table 2. Inflow conditions for the prototype case—Guxian Reservoir.

Wubu station, Yellow River		Baijiachuan station, Wuding River	
Q_{mi} (m^3/s)	C_{mi}	Q_{ti} (m^3/s)	C_{ti}
3,600	0.069	Time series for July 2017 flood, Fig. 13	

Fig. 13. Guxian Reservoir study: observed data and piece-wise linear approximations of

flow discharge hydrograph and volumetric sediment concentration time series at Baijiachuan station for a super-concentrated flood lasting from 0:00 a.m. July 26 to 0:00 a.m. July 29, 2017.

The following parameters are specified based on data from the middle Yellow River: mean sediment particle size $d = 25\,\mu\mathrm{m}$, bed sediment porosity $p = 0.4$, and sediment density $\rho_s = 2{,}650$ kg/m^3. The computational grid is uniform with 35 m spacing in both longitudinal and lateral directions, and the total number of mesh cells is 3,905,839. The Courant number is set to 0.4. In the ODL model, the bed roughness Manning's coefficient, n_b, is set to $0.03\,\mathrm{m}^{-1/3}\cdot\mathrm{s}$; in the proposed EDL model the yield stress and dynamic viscosity are estimated using Eqs. (20) and (21) with $\phi = 0.7$. In both models, the interface roughness Manning coefficient, n_i, is set to 0.005 m$^{-1/3}\cdot$s following Cao et al. (2015).

4.3. Results and discussion

Here the influence of the rheological characteristics on the formation and propagation of reservoir turbidity currents and bed deformation in the Guxian Reservoir domain are examined based on simulations using the proposed EDL model and the ODL model. In general, the transition from subaerial open channel sediment-laden flow to subaqueous turbid flow features the formation of a reservoir turbidity current with unstable plunge points that propagate forward. Figs.14(c) and 14(d) show that by t = 12 h, the subaerial sediment-laden flows in the main channel (MC) and Wuding River (WR) have plunged into clear water and formed turbidity currents, whilst the front of the WR turbidity current has intruded into the MC and propagated both upstream and downstream simultaneously. By t = 24 h, the front of the WR turbidity current has mixed with the MC turbidity current and is propagating downstream with a high interface elevation at the junction (Figs. 14(e) and 14(f)). At t = 48 h, as the sediment input from the WR decreases, the thickness of the turbidity current increases in the WR (Figs. 14(g) and 14(h)). This primarily occurs because Ri reduces progressively with the lowering sediment concentration, and thus, induces greater water entrainment, E_{w}. At t = 72 h, the plunge point is located downstream the junction in the MC, and the upper clear-water layer in the WR disappears (Figs. 14(i) and 14(j)). Moreover, as it is slowing, the MC turbidity current has not yet arrived at the Guxian Dam. This is because the sediment input from the WR decreases, and sedimentation occurs within WR and near the river confluence (Fig. 15), which correspondingly reduces both the density and the driving force of the turbidity currents.

The EDL and ODL model results display pronounced differences in the hydro-sediment-morphological processes associated with hyperconcentrated turbidity currents. When the sediment concentration of the turbidity current exceeds the threshold concentration, c_{vo}, of the non-Newtonian fluid, the bed boundary resistance computed using the EDL model is larger than that computed using the ODL model (Figs. 16(a) and 16(b)). Hence, the propagation of the turbidity current predicted by the proposed EDL model is slower than that predicted by the ODL model (Figs. 14(c) and 14(d), Fig. S8 in the Supporting Materials). However, after $t \approx 12$ h, the sediment concentration of the reservoir turbidity current falls below the threshold concentration, c_{vo} (Fig. S9 in the Supporting Materials). This means that the turbidity current gradually dilutes, and its behavior approaches that of a Newtonian flow. Notably, the proposed EDL model predicts larger bed aggradation at the confluence than does the ODL model (Figs. 15(a) and 15(b)). In response to the greater boundary resistance, the decreasing velocity of the turbidity current lowers the sediment entrainment flux, leading to reduced sediment concentrations and a smaller driving force for the turbidity current. Therefore, the hyperconcentrated turbidity current predicted by the proposed EDL model features slower propagation and more significant sedimentation than that predicted by the ODL model.

Fig. 14. Guxian Reservoir study: water surface, interface, and bed profiles along the thalweg of (a, c, e, g, i) the main channel (MC) and (b, d, f, h, j) the Wuding River (WR) computed using the ODL and proposed EDL models at time t = 0, 12, 24, 48, and 72 h, respectively.

Fig. 15. Guxian Reservoir study: contours of bed deformation depth $\Delta z_{\mathrm{b}} = z_{\mathrm{b}}(x, y, t) - z_{\mathrm{b}}(x, y, 0)$ at time $t = 72\,\mathrm{h}$ predicted by (a) the proposed EDL model and (b) the ODL model.

Fig. 16. Guxian Reservoir study: distributions of bed shear stress, τ_{eff}, at time t = 12 and 72 h, predicted using (a, c) the proposed EDL model and (b, d) the ODL model.

5. Conclusions

A two-dimensional double layer-averaged model has been proposed that incorporates non-Newtonian constitutive properties of yield stress and shear-thinning, and resolves the holistic physical processes behind the formation and propagation of turbidity currents. Both Newtonian (ODL) and non-Newtonian (EDL) models were applied to simulate hyperconcentrated subaerial mud flows, subaqueous debris flows, and reservoir turbidity currents. For hyperconcentrated turbidity currents, it was found that as the yield stress, τ_{Y}, decreases to zero, the non-Newtonian flow transforms into a Newtonian flow. The power coefficient, n, which represents shear-thinning or shear-thickening phenomena, plays a key role in the large range of shearing rates encountered in non-Newtonian flows. Increasing power coefficient, n, leads to larger turbidity current thickness and slower propagation. Interface interactions between the subaqueous non-Newtonian flow underlayer and ambient water overlayer play a critical part in the evolution of the turbidity current. Water entrainment causes both the front thickness and final runout distance of a non-Newtonian turbidity current to increase, whereas interfacial resistance has a secondary effect. Hardly any sedimentation occurs in a non-Newtonian flow carrying fine particles, as would be expected.

The proposed EDL model and ODL model predict very similar behavior for dilute concentrated turbidity currents, confirming that the EDL model is effectively the same as an ODL model in cases where non-Newtonian behavior is negligible. When sediment concentration exceeds a threshold value, pronounced differences develop between the predictions made using the EDL and ODL models of the evolution of a hyperconcentrated turbidity current. Unlike the Newtonian model, the proposed EDL model predicts slower propagation of the turbidity current and more significant bed aggradation, causing a feedback effect on the evolution of the turbidity current through decreased turbidity current density and, thus, reduced driving force.

The current findings demonstrate that it is essential to account for non-Newtonian rheology when modeling a hyperconcentrated turbidity current. This has significant implications for the simulation of hydro-sediment-morphological processes, and, therefore, sediment management of reservoirs in sediment-laden river basins. Moreover, in a turbidity current with uniform sediment, the particle diameter has an inherent impact on bed deformation. In this regard, more refined entrainment modes of sufficiently fine cohesive sediment are warranted for incorporation into the proposed model, which will be done in future investigations.

Acknowledgments

This research has been funded by the National Natural Science Foundation of China under Grant No. 12072244. Special thanks go to the Yellow River Institute of Hydraulic Research and Key Laboratory of Yellow River Sediment Research, Zhengzhou, China, for their support on the experimental data in Section 3.2.

References

Adebiyi, A. A., & Hu, P. (2021). A numerical study on impacts of sediment erosion/deposition on debris flow propagation. *Water*, *13*, 1968.

Balmforth, N. J., & Provenzale, A. (2010). *Geomorphological fluid mechanics*. Berlin: Springer.

Brufau, P., Garcia-Navarro, P., Ghilardi, P., Natale, L., & Savi, F. (2000). 1D mathematical modelling of debris flow. *Journal of Hydraulic Research*, *38*(6), 435–446.

Cao, Z. X., Pender, G., & Carling, P. (2006). Shallow water hydrodynamic models for hyperconcentrated sediment-laden floods over erodible bed. *Advances in Water Resources*, *29*(4), 546–557.

Cao, Z. X., Li, J., Pender, G., & Liu, Q. Q. (2015). Whole-process modeling of reservoir turbidity currents by a double layer-averaged model. *Journal of Hydraulic Engineering*, *141*(2), 04014069.

Denlinger, R. P., & Iverson, R. M. (2001). Flow of variably fluidized granular masses across three-dimensional terrain 2. Numerical predictions and experimental tests. *Journal of Geophysical Research*, *106*(B1), 553–566.

Fedele, J. J., & García, M. H. (2009). Laboratory experiments on the formation of subaqueous depositional gullies by turbidity currents. *Marine Geology*, *258*(1), 48–59.

Fei, X. J. (1991). A model for calculating viscosity of sediment carrying flow in the middle and lower Yellow River. *Journal of Sediment Research*, *6*(2), 1–13. *(in Chinese)*

Georgoulas, A. N., Angelidis, P. B., Panagiotidis, T. G., & Kotsovinos, N. E. (2010). 3D numerical modelling of turbidity currents. *Environmental Fluid Mechanics*, *10*(6), 603–635.

Guo, Q. C., Hu, C. H., Takeuchi, K., Ishidaira, H., Cao, W. H., & Mao, J. X. (2008). Numerical modeling of hyper-concentrated sediment transport in the lower Yellow River. *Journal of Hydraulic Research*, *46*(5), 659–667.

Hallworth, M. A., & Huppert, H. E. (1998). Abrupt transitions in high-concentration, particle-driven gravity currents. *Physics of Fluids*, *10*(5), 1083–1087.

Hou, J. M., Simons, F., Mahgoub, M., & Hinkelmann, R. (2013). A robust well-balanced model on unstructured grids for shallow water flows with wetting and drying over complex topography. *Computer Methods in Applied Mechanics and Engineering*, *257*, 126–149.

Hu, P., Cao, Z. X., Pender, G., & Tan, G. M. (2012). Numerical modelling of turbidity currents in the Xiaolangdi Reservoir, Yellow River, China. *Journal of Hydrology*, *464–465*, 41–53.

Hu, P., & Li, Y. (2020). Numerical modeling of the propagation and morphological changes of turbidity currents using a cost-saving strategy of solution updating. *International Journal of Sediment Research*, *35*(6), 587–599.

Huang, X., & Garcia, M. H. (1997). A perturbation solution for Bingham-plastic mudflows. *Journal of Hydraulic Engineering*, *123*(11), 986–994.

Imran, J., Parker, G., Locat, J., & Lee, H. (2001). 1D numerical model of muddy subaqueous and subaerial debris flows. *Journal of Hydraulic Engineering*, *127*(11), 959–968.

Jacobson, M. R., & Testik, F. Y. (2013). On the concentration structure of high-concentration constant-volume fluid mud gravity currents. *Physics of Fluids*, *25*(1), 016602.

Johnson, C. G., Kokelaar, B. P., Iverson, R. M., Logan, M., LaHusen, R. G., & Gray, J. M. N. T. (2012). Grain-size segregation and levee formation in geophysical mass flows. *Journal of Geophysical Research*, *117*, F01032.

Lai, Y. G., Huang, J., & Wu, K. (2015). Reservoir turbidity current modeling with a two-dimensional layer-averaged model. *Journal of Hydraulic Engineering*, *141*(12), 04015029.

Lee, H. Y., & Yu, W. S. (1997). Experimental study of reservoir turbidity current. *Journal of Hydraulic Engineering*, *123*(6), 520–528.

Li, J., Cao, Z. X., Pender, G., & Liu, Q. Q. (2013). A double layer-averaged model for dam-break flows over mobile bed. *Journal of Hydraulic Research*, *51*(5), 518–534.

Li, J., Cao, Z. X., Pender, G., & Liu, Q. Q. (2015). Hyperbolicity analysis of a double layer-averaged model for open-channel sediment-laden flows. *Scientia Sinica: Physica, Mechanica ＆ Astronomica*, *45*(10), 104705. *(in Chinese)*

Li, J., Cao, Z. X., & Liu, Q. Q. (2019). Waves and sediment transport due to granular landslides impacting reservoirs. *Water Resources Research*, *55*(1), 495–518.

Li, J., Cao, Z. X., Cui, Y., & Borthwick, A. (2020). Barrier lake formation due to landslide impacting a river: A numerical study using a double layer-averaged two-phase flow model. *Applied Mathematical Modelling*, *80*, 574–601.

Li, J., Cao, Z. X., Cui, Y., Fan, X., Yang, W. J., Huang, W., & Borthwick, A. (2021). Hydro-sediment-morphodynamic processes of the baige landslide-induced barrier Lake, Jinsha River, China. *Journal of Hydrology*, *596*, 126–134.

Locat, J. (1997). Normalized rheological behaviour of fine muds and their flow properties in a pseudoplastic regime. In: C.-L. Chen (Ed.), *Debris-flow hazard mitigation: Mechanics, prediction, and assessment*, (pp. 260–269), Reston, VA, USA: American Society of Civil Engineers.

O'Brien, J. S., & Julien, P. Y. (1988). Laboratory analysis of mudflow properties. *Journal of Hydraulic Engineering*, *114*(8), 877–887.

Parker, G., Fukushima, Y., & Pantin, H. M. (1986). Self-accelerating turbidity currents. *Journal of Fluid Mechanics*, *171*(3), 145–181.

Pierson, T. C., & Scott, K. M. (1985). Downstream dilution of a lahar: Transition from debris flow to hyperconcentrated streamflow. *Water Resources Research*, *21*(10), 1511–1524.

Qian, X. S., Xu, J. P., Das, H. S., Wang, D. W., & Bai, Y. (2020). Improved modeling of subaerial and subaqueous muddy debris flows. *Journal of Hydraulic Engineering*, *146*(7), 06020007.

Richardson, J. F., & Zaki, W. N. (1997). Sedimentation and fluidisation: Part 1. *Chemical Engineering Research & Design*, *32*, S82–S100.

Toro, E. F. (2001). *Shock-capturing methods for free-surface shallow flows*. Chichester, UK: Wiley.

Wang, T., Wang, Y. J., Ma, H. B., Li, T., Ren, Z. H., & Wang, Z. L. (2020). Experimental study on flow and sediment evolution characteristics in conjunction area after confluence of density current at reservoir tributary. *Yellow River*, *42*(5), 56–61. *(in Chinese)*

Wang, W., Chen, G., Han, Z., Zhou, S., Zhang, H., & Jing, P. (2016). 3D numerical simulation of debris-flow motion using SPH method incorporating non-Newtonian fluid behavior. *Natural Hazards*, *81*(3), 1981–1998.

Wang, Z. Y., Qi, P., & Melching, C. S. (2009). Fluvial hydraulics of hyperconcentrated floods in Chinese rivers. *Earth Surface Processes and Landforms*, *34*, 981–993.

Wang, Z. Y., Wu, B. S., & Wang, G. Q. (2007). Fluvial processes and morphological response in the Yellow and Weihe Rivers to closure and operation of Sanmenxia Dam. *Geomorphology*, *91*(1–2), 65–79.

Wang, Z., Xia, J., Li, T., Deng, S., & Zhang, J. (2016). An integrated model coupling open-channel flow, turbidity current and flow exchanges between main river and tributaries in Xiaolangdi Reservoir, China. *Journal of Hydrology*, *543*, 548–561.

Wang, Z., Xia, J., Zhang, J., & Li, T. (2018). Modeling turbidity currents in the Xiaolangdi Reservoir with the effect of flow exchanges with tributaries. *Advanced Engineering Sciences*, *50*(1), 85–93. *(in Chinese)*

Wright, L. D., Wiseman, W. J., Bornhold, B. D., Prior, D. B., Suhayda, J. N., Keller, G. H., … Fan, Y. B. (1988). Marine dispersal and deposition of Yellow River silts by gravity-driven underflows. *Nature*, *332*, 629–632.

Wright, V. G. (1987). *Laboratory and numerical study of mud and debris flow (Ph.D. dissertation)*, Civil Engineering, University of California at Davis, Davis, CA, USA.

Wu, W. M. (2007). *Computational river dynamics*. London: Taylor and Francis.

Xia, C. C., & Tian, H. Y. (2022). A quasi-single-phase model for debris flows incorporating non-Newtonian fluid behavior. *Water*, *14*, 1369.

Zhang, R. J., & Xie, J. H. (1993). *Sedimentation research in China: Systematic selections*. Beijing: China Water & Power Press. *(in Chinese)*

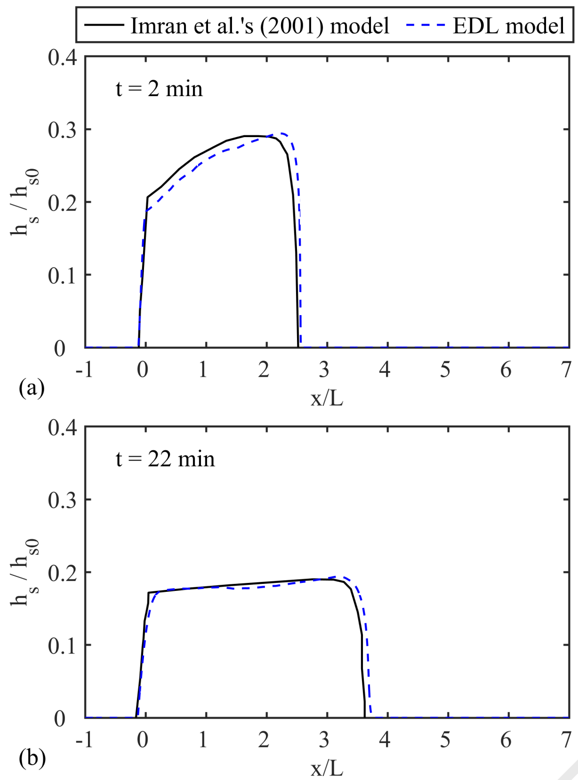

Imran et al.'s (2001) model
EDL model
t = 2 min
t = 22 min
h_s / h_s0
x/L
(a)
(b)
0.4
0.3
0.2
0.1
0
-1
0
1
2
3
4
5
6
7

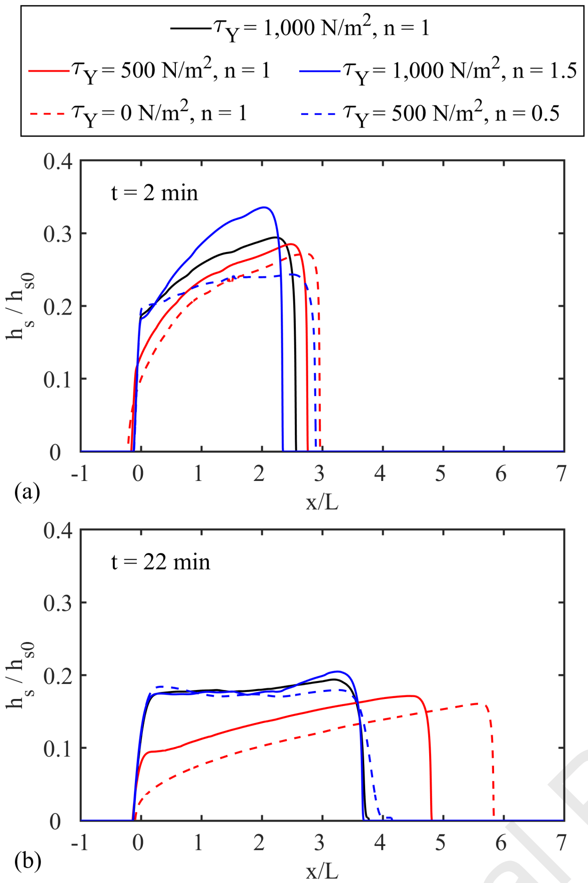

τ_Y = 1,000 N/m^2, n = 1
τ_Y = 500 N/m^2, n = 1
τ_Y = 1,000 N/m^2, n = 1.5
τ_Y = 0 N/m^2, n = 1
τ_Y = 500 N/m^2, n = 0.5
t = 2 min
t = 22 min
h_s / h_{s0}
x/L
(a)
(b)

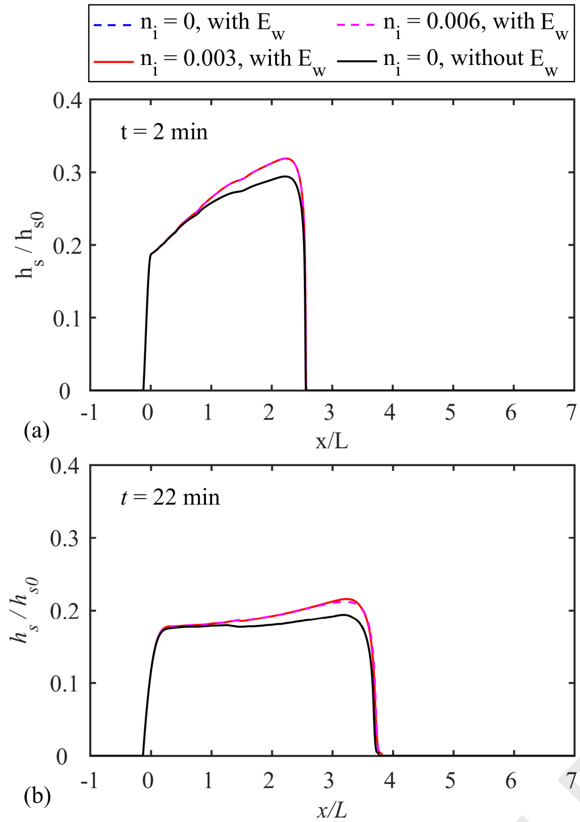
n_i = 0, with E_w
n_i = 0.006, with E_w
n_i = 0.003, with E_w
n_i = 0, without E_w
t = 2 min
h_s / h_s0
x/L
(a)
t = 22 min
h_s / h_s0
x/L
(b)

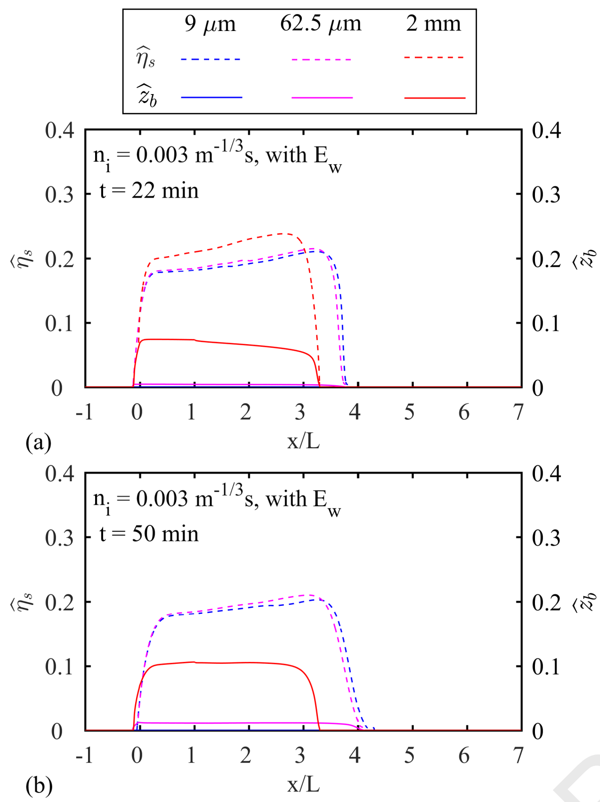
9 μm
62.5 μm
2 mm
$\widehat{\eta}_s$
$\widehat{z}_b$
n_i = 0.003 $m^{-1/3}$s, with E_w
t = 22 min
t = 50 min
x/L
(a)
(b)

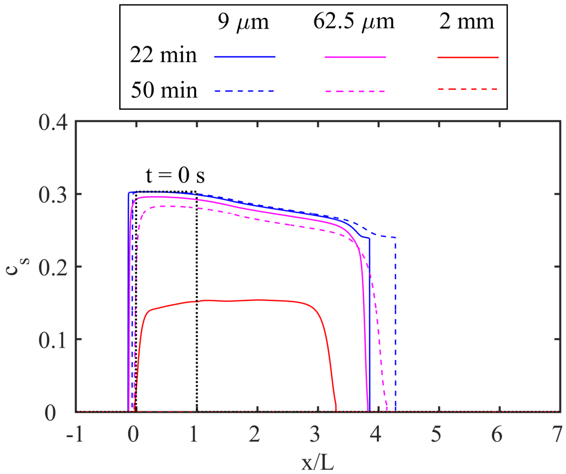
9 μm
62.5 μm
2 mm
22 min
50 min
t = 0 s
0.4
0.3
0.2
0.1
0
c_s
-1
0
1
2
3
4
5
6
7
x/L

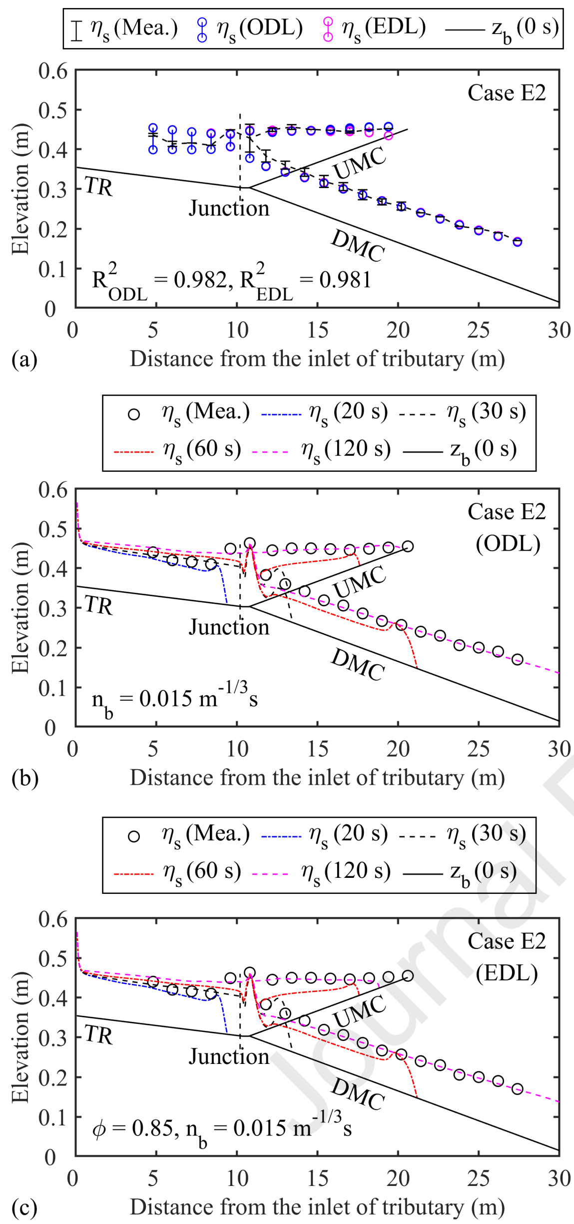

(a)
η_s (Mea.) η_s (ODL) η_s (EDL) z_b (0 s)
Case E2
TR
Junction
UMC
DMC
$R^2_{ODL} = 0.982$, $R^2_{EDL} = 0.981$
Elevation (m)
Distance from the inlet of tributary (m)
(b)
η_s (Mea.) η_s (20 s) η_s (30 s) η_s (60 s) η_s (120 s) z_b (0 s)
Case E2 (ODL)
$n_b = 0.015\ m^{-1/3}s$
(c)
Case E2 (EDL)
$\phi = 0.85$, $n_b = 0.015\ m^{-1/3}s$

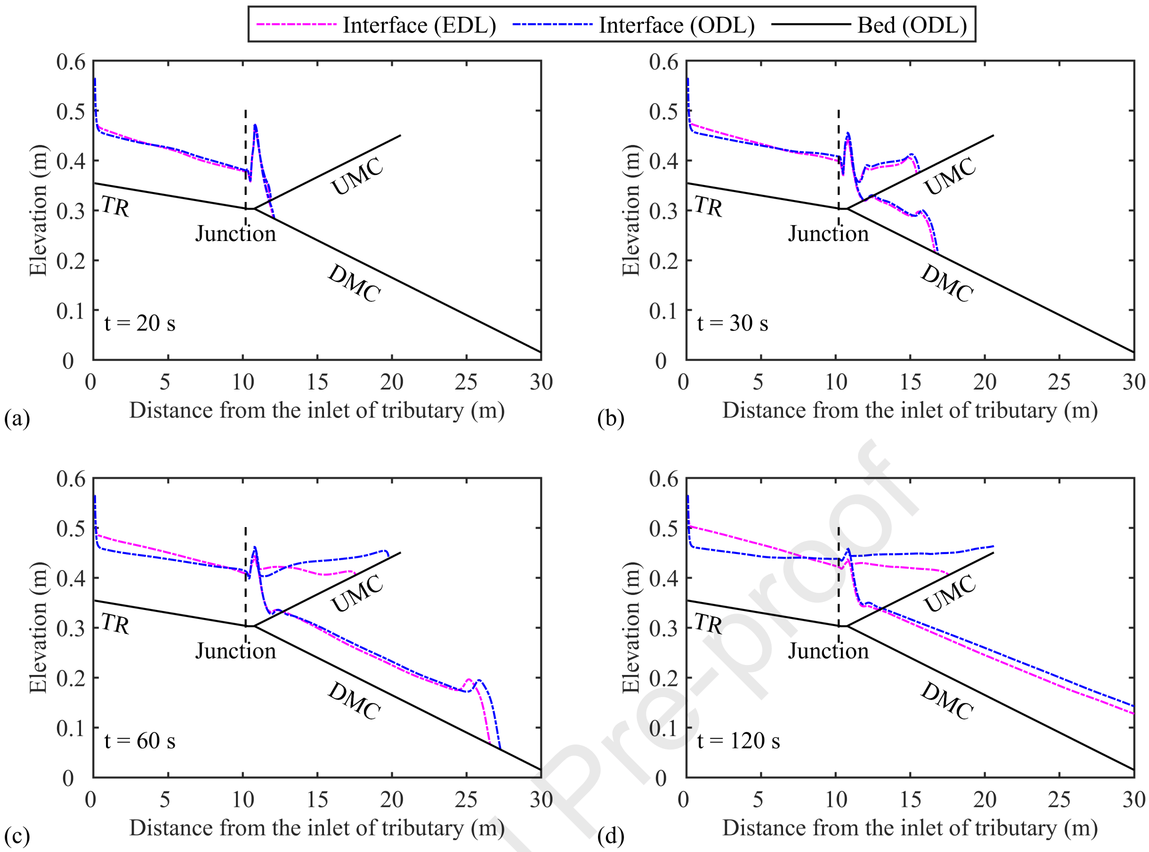
Interface (EDL)
Interface (ODL)
Bed (ODL)
Elevation (m)
Distance from the inlet of tributary (m)
TR
Junction
UMC
DMC
t = 20 s
t = 30 s
t = 60 s
t = 120 s
(a)
(b)
(c)
(d)

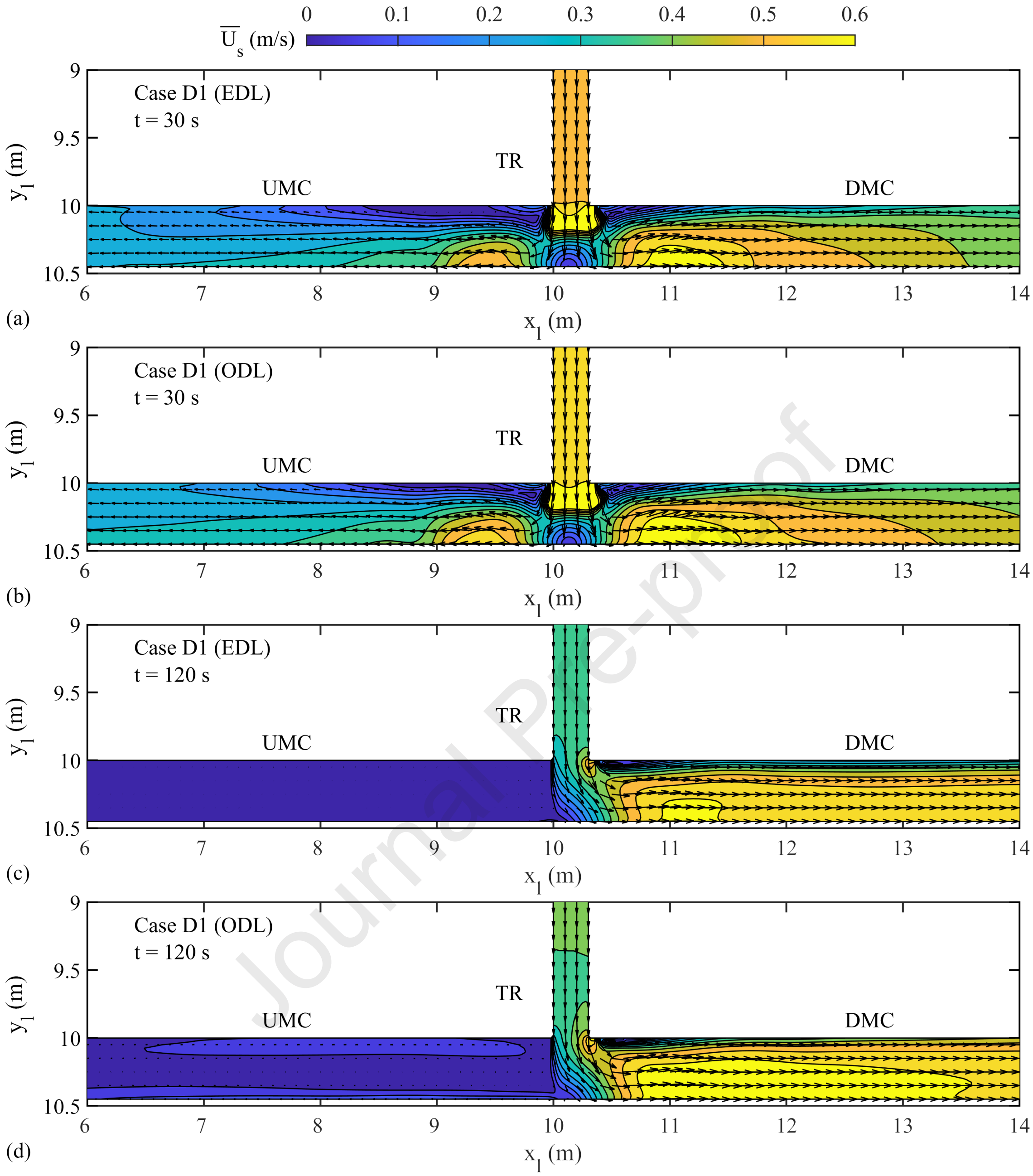

$\overline{U}_s$ (m/s)
0
0.1
0.2
0.3
0.4
0.5
0.6
Case D1 (EDL)
t = 30 s
TR
UMC
DMC
y_1 (m)
x_1 (m)
(a)
Case D1 (ODL)
t = 30 s
(b)
Case D1 (EDL)
t = 120 s
(c)
Case D1 (ODL)
t = 120 s
(d)

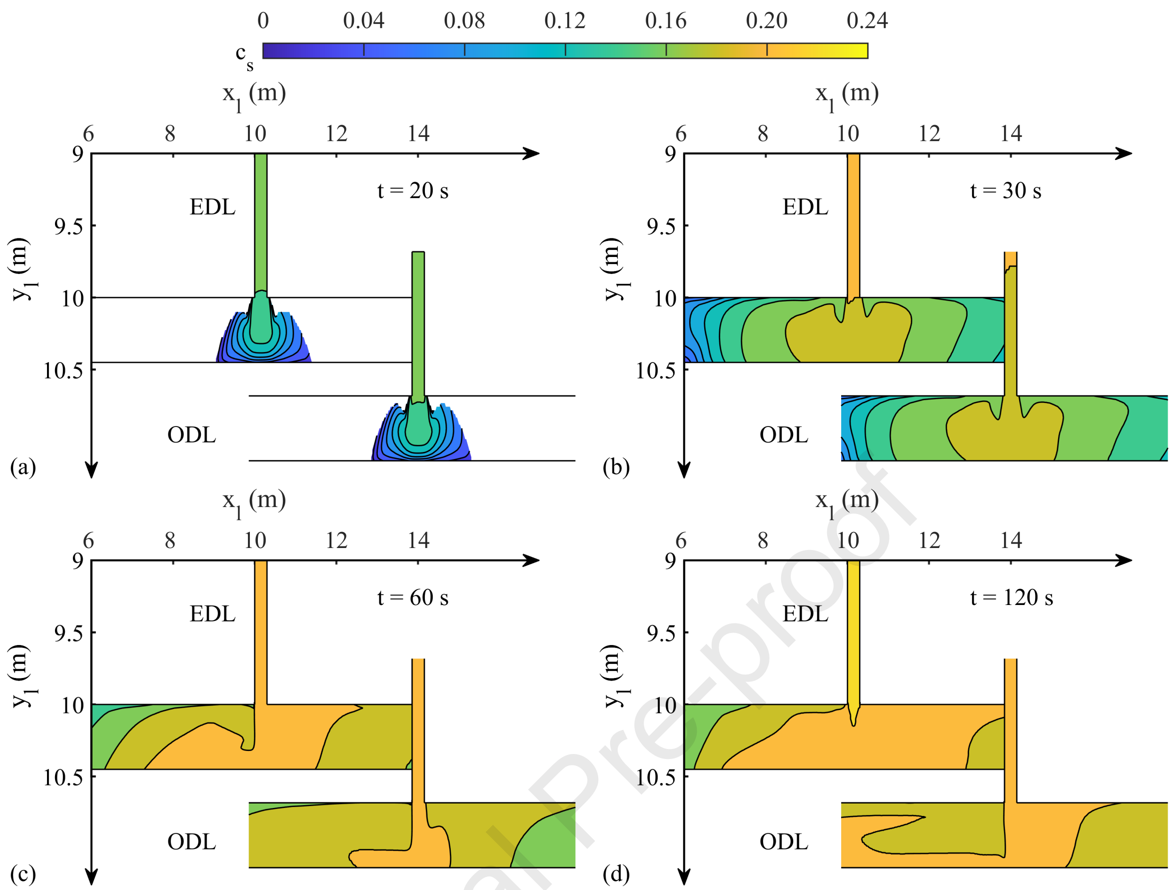

0
0.04
0.08
0.12
0.16
0.20
0.24
c_s
x_1 (m)
6
8
10
12
14
9
9.5
10
10.5
y_1 (m)
EDL
ODL
t = 20 s
(a)
t = 30 s
(b)
t = 60 s
(c)
t = 120 s
(d)

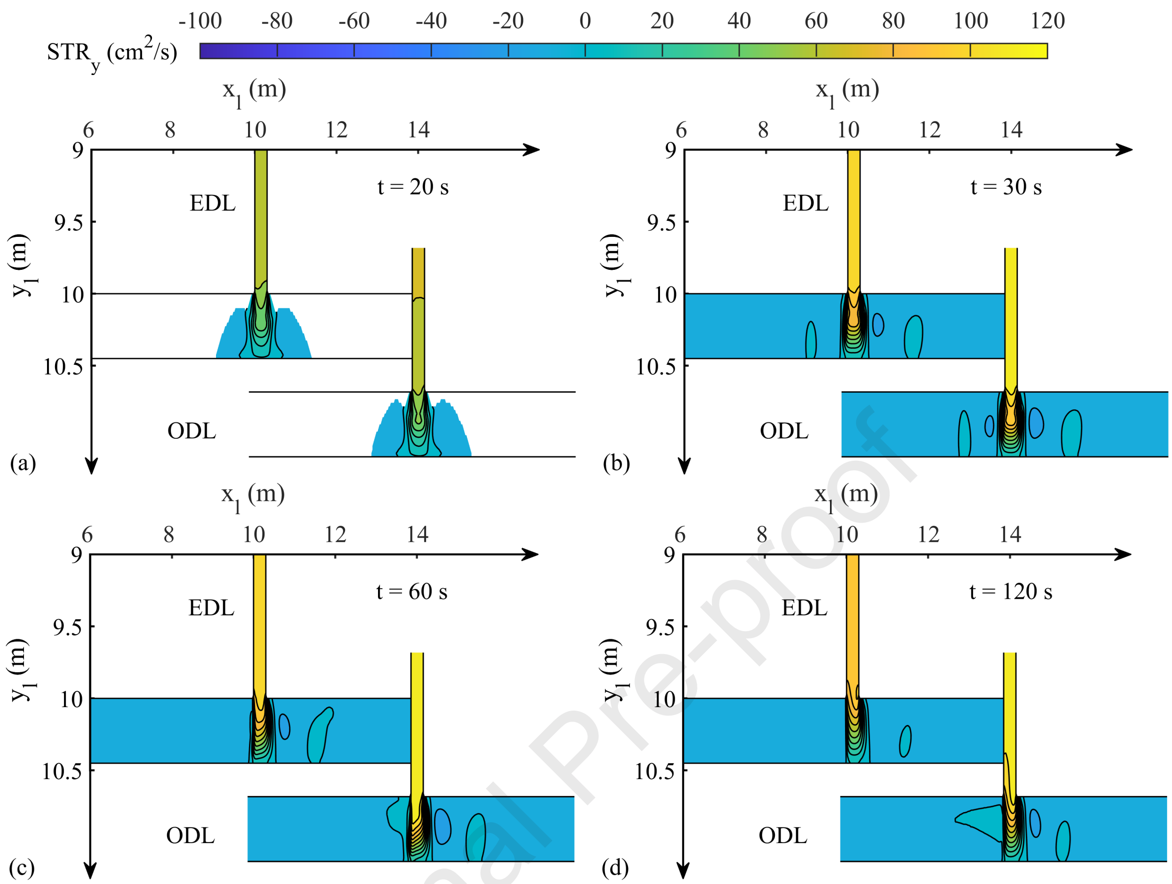

STR$_y$ (cm^2/s)
-100 -80 -60 -40 -20 0 20 40 60 80 100 120
x$_1$ (m)
y$_1$ (m)
EDL
ODL
t = 20 s
t = 30 s
t = 60 s
t = 120 s
(a)
(b)
(c)
(d)

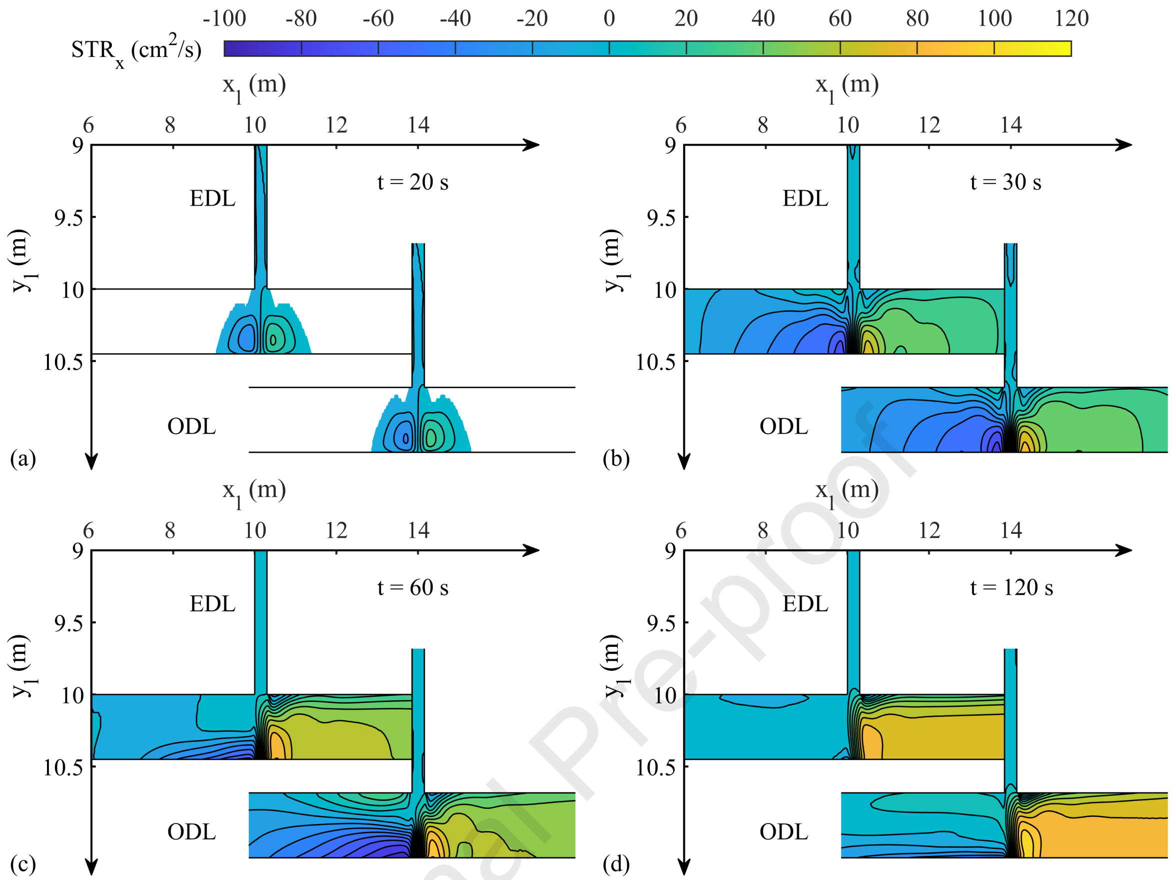
-100 -80 -60 -40 -20 0 20 40 60 80 100 120
STR$_x$ (cm^2/s)
x$_1$ (m)
y$_1$ (m)
6 8 10 12 14
9 9.5 10 10.5
EDL
ODL
t = 20 s
t = 30 s
t = 60 s
t = 120 s
(a)
(b)
(c)
(d)

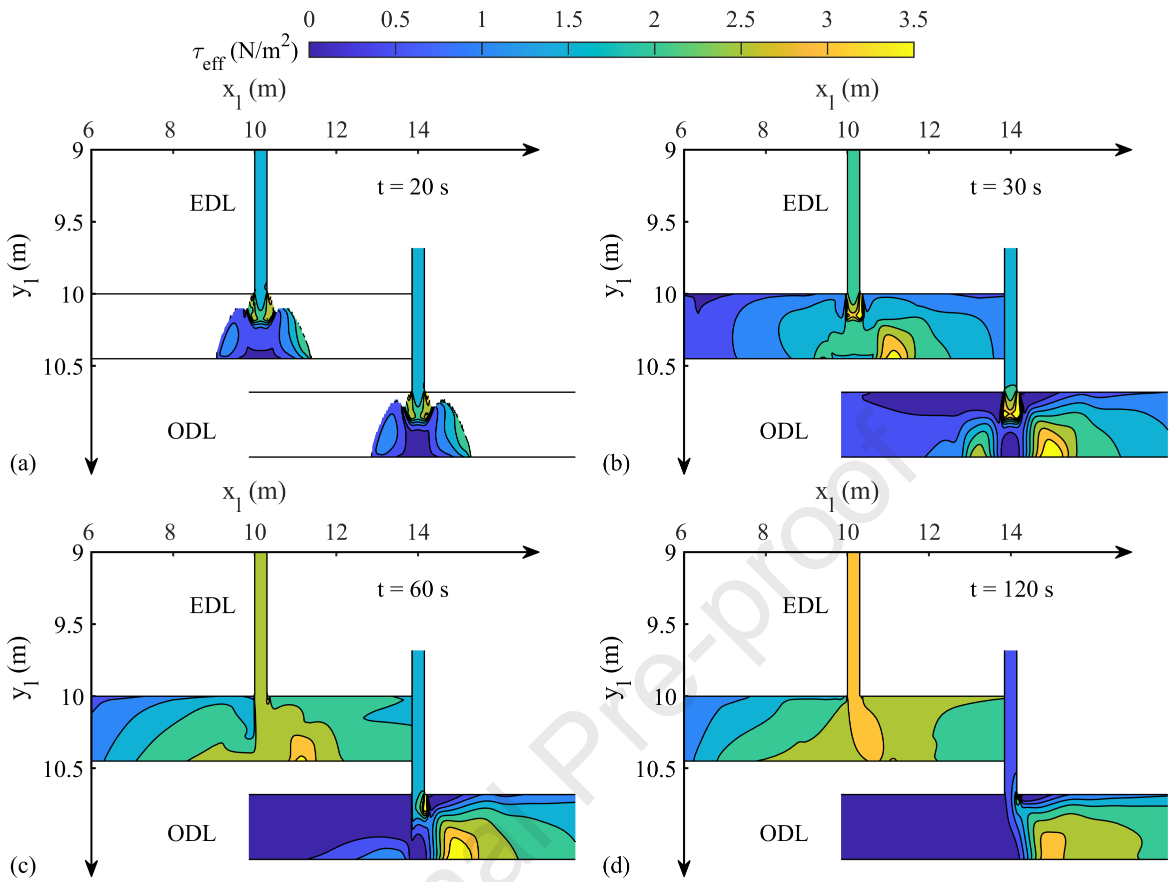

τ_{eff} (N/m^2)
0
0.5
1
1.5
2
2.5
3
3.5
x$_1$ (m)
y$_1$ (m)
6
8
10
12
14
9
9.5
10
10.5
EDL
ODL
t = 20 s
t = 30 s
t = 60 s
t = 120 s
(a)
(b)
(c)
(d)

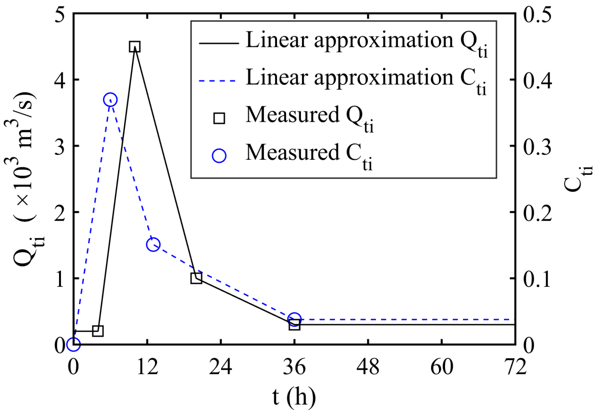
Linear approximation Q_{ti}
Linear approximation C_{ti}
Measured Q_{ti}
Measured C_{ti}
Q_{ti} ($\times 10^3$ m^3/s)
C_{ti}
t (h)
0
12
24
36
48
60
72
0
1
2
3
4
5
0
0.1
0.2
0.3
0.4
0.5

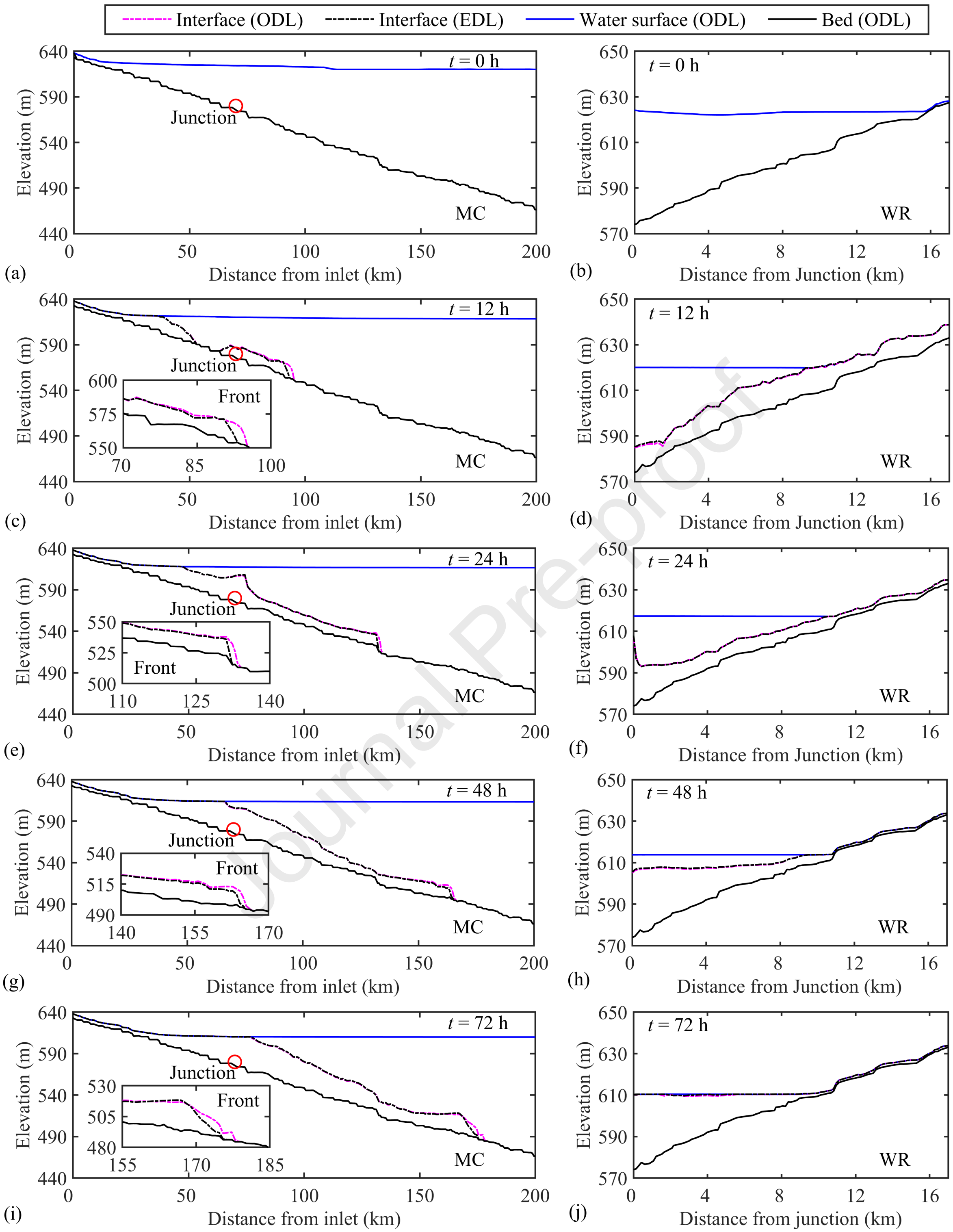
Interface (ODL)
Interface (EDL)
Water surface (ODL)
Bed (ODL)
t = 0 h
t = 12 h
t = 24 h
t = 48 h
t = 72 h
Junction
Front
MC
WR
Elevation (m)
Distance from inlet (km)
Distance from Junction (km)
Distance from junction (km)
(a)
(b)
(c)
(d)
(e)
(f)
(g)
(h)
(i)
(j)

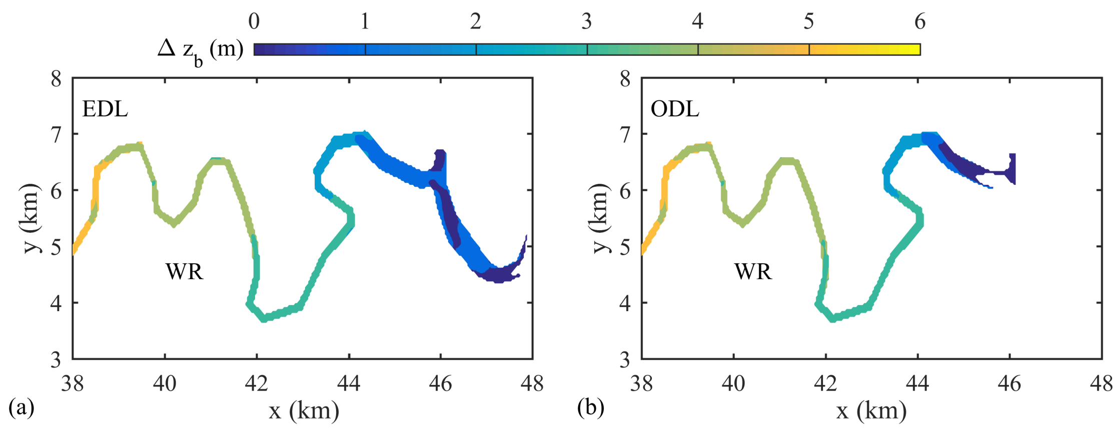

Δ z_b (m)
0
1
2
3
4
5
6
EDL
ODL
WR
y (km)
x (km)
(a)
(b)

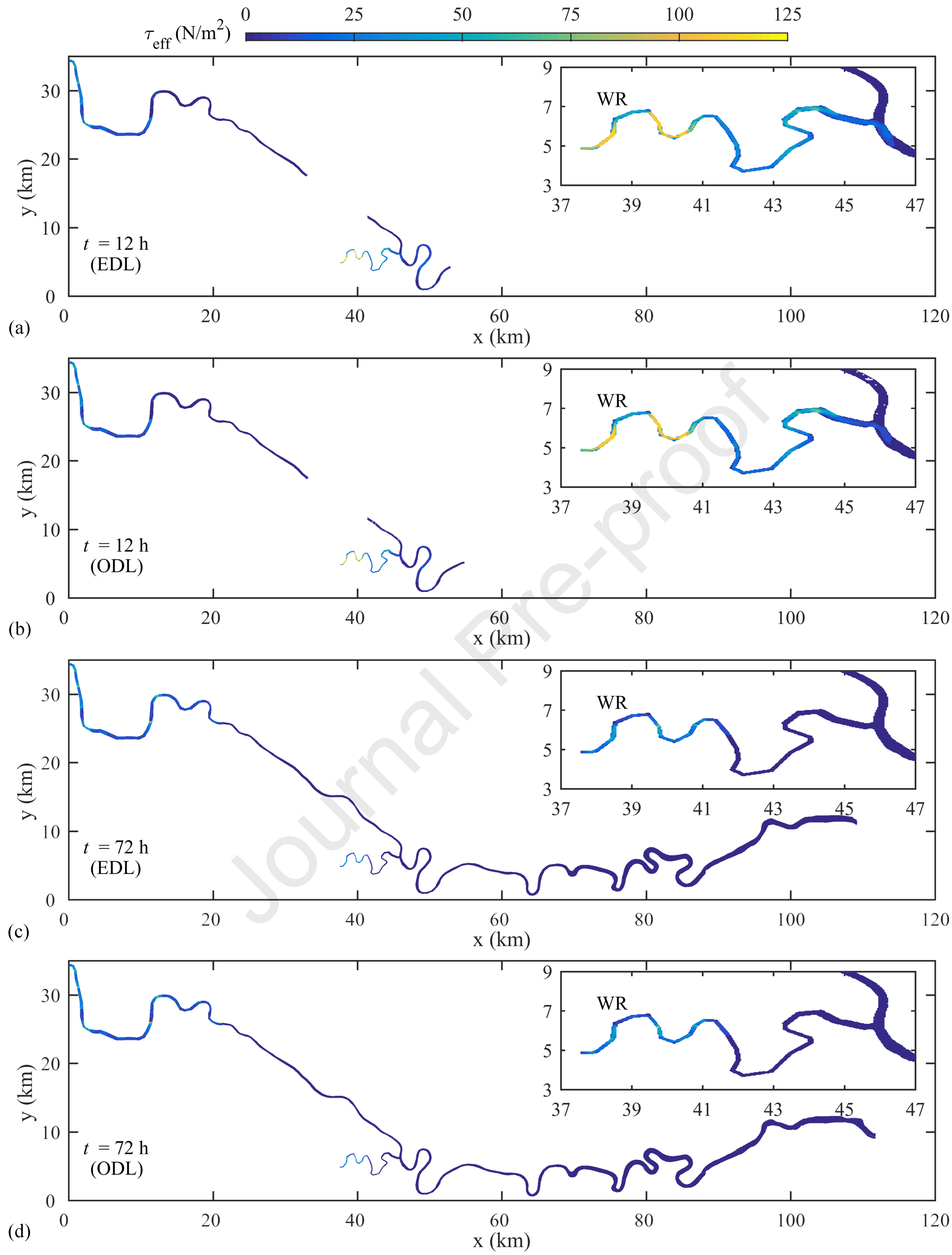
τ_{eff} (N/m^2)
0
25
50
75
100
125
y (km)
x (km)
t = 12 h
(EDL)
(ODL)
t = 72 h
WR
(a)
(b)
(c)
(d)

Declaration of interests

☑ The authors declare that they have no known competing financial interests or personal relationships that could have appeared to influence the work reported in this paper.

☐The authors declare the following financial interests/personal relationships which may be considered as potential competing interests: